

## Article

# The Influence of Tool Geometry Parameters on Thermo-Mechanical Loads and Residual Stresses Induced by Orthogonal Cutting of AA6061-T6: A Numerical Investigation

Sandrine A. Tcheuhebou Tina, Mahshad Javidikia, Mohammad Jahazi  and Victor Songmene \* 

Department of Mechanical Engineering, École de Technologie Supérieure (ÉTS), 1100 Notre-Dame Street West, Montréal, QC H3C 1K3, Canada

\* Correspondence: victor.songmene@etsmtl.ca; Tel.: +1-514-396-8869; Fax: +1-514-396-8530

**Abstract:** The residual stresses state that a mechanical part obtained after machining is a crucial factor that impacts its in-service performance. This stress state is influenced by the thermomechanical loads exerted on the parts during the machining process, which are, in turn, determined by the tool parameters, process, and machining conditions. The aim of the present research was to anticipate how the cutting tool's edge radius, rake angle, and clearance angle would affect the forces, temperature, and residual stresses induced while orthogonally cutting aluminum AA6061-T6. To achieve this, two-dimensional DEFORM<sup>TM</sup> software was utilized to develop a finite element model. The residual stresses trend results obtained demonstrated that rake angles of 0° and 17.5–20° values with a small edge radius (5 to 10 μm) and clearance angles of 7 and 17.5° values gave higher compressive stresses. The obtained simulated results were in good agreement with the experiments. The cutting forces, the temperature, and the maximum and minimum machining-induced residual stresses were found to be influenced more by the tool edge radius and the tool rake angle. The influence of the clearance angles on the above-mentioned machining responses was the least. Residual stresses can have a significant impact on the in-service performance of machined parts. The obtained results will help engineers select or design tools that promote a desired surface integrity during machining. This task is not obvious in practice because of difficulties in measuring residual stresses and also because the machining parameters and the tool geometry parameters have different and opposite impacts on thermo-mechanical loads, productivity, and on machining induced residual stresses.

**Keywords:** orthogonal cutting; tool geometry; residual stresses; 2D FE simulations; aluminum



**Citation:** Tcheuhebou Tina, S.A.; Javidikia, M.; Jahazi, M.; Songmene, V. The Influence of Tool Geometry Parameters on Thermo-Mechanical Loads and Residual Stresses Induced by Orthogonal Cutting of AA6061-T6: A Numerical Investigation. *Processes* **2023**, *11*, 996. <https://doi.org/10.3390/pr11040996>

Academic Editors: Jun Zhang, Kuo Liu and Hongguang Liu

Received: 10 February 2023  
Revised: 16 March 2023  
Accepted: 21 March 2023  
Published: 24 March 2023



**Copyright:** © 2023 by the authors. Licensee MDPI, Basel, Switzerland. This article is an open access article distributed under the terms and conditions of the Creative Commons Attribution (CC BY) license (<https://creativecommons.org/licenses/by/4.0/>).

## 1. Introduction

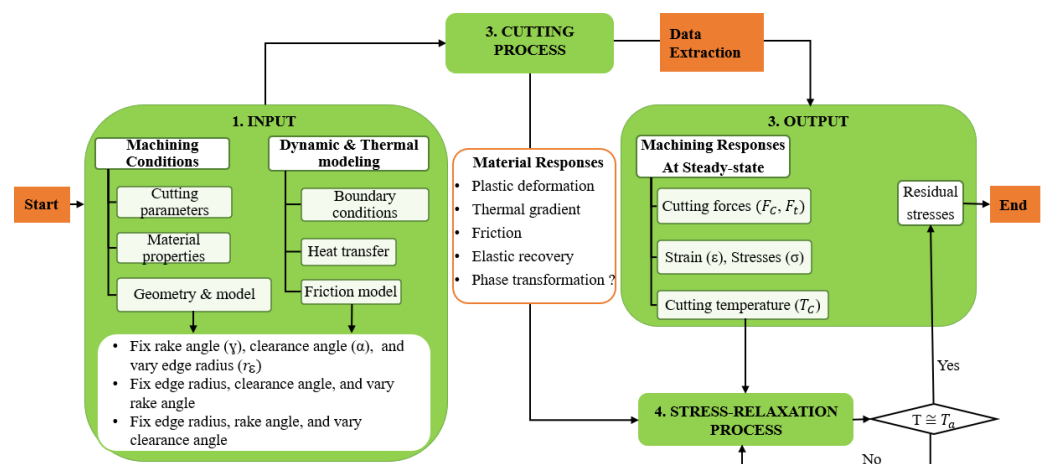
AA6061-T6 is a heat-treated (artificially aged) aluminum alloy (AA) that is widely used in transportation, construction, and engineering industries in many applications. AA6061-T6 is popularly used to make aeronautical, automobiles, ships, and motorcycles components (frames, body, and rotor); to create building/house/bridges structures; and for many mechanical fittings and equipment such as rotor, rivets, towers, boilers, boats, etc. [1]. Its popularity is due to their low weight-to-size ratio, excellent light-to-weight ratio, good corrosion resistance, formability, weldability, and wettability [2].

Aluminum alloys have generally good machinability [2] but during the cutting of ductile alloys such AA6061-T6, there is a risk of the formation of a built-up edge that can modify the tool geometry and deteriorate the machine part surface finish [2]. Other machining induced damages involve tiny cracks that can propagate throughout the workpiece and therefore decrease its life span. The quality of the machined surface and subsurface can be appreciated by its surface integrity, including the surface roughness, microstructure, and residual stresses. These machining responses are influenced by the machining conditions, machining environment, workpiece material, and tool geometry [3–5]. Table 1 presents some typical tool geometries (rake angles and clearance angles) for machining aluminum alloys.

**Table 1.** Typical tool geometries used for machining aluminum alloys.

Refs.	Authors (Year)	Material/ Operation	Rake Angle [°]	Clearance Angle [°]
[5]	Javidikia et al. (2020)	AA6061-T6 Orthogonal turning	−8 to +8	7
[6]	Ravikanth et al. (2022)	AA2219 Turning	20	0
[7]	Casuso et al. (2022)	AA2024-T3 Milling	18	9
[8]	Daoud et al. (2015)	AA2024-T351 Orthogonal turning	−8 to +8	11
[9]	Patel (2018)	AA2024-T351 Orthogonal turning	−3 to +20	-

The machined part surface integrity can be determined through experiments and/or simulations [10,11]. The measurement of residual stresses on large pieces is a delicate problem. Some difficulties come from measurement errors as noted by Aurrekoetxa et al. [12] and others from the fact that this procedure is destructive (holes methods and slice-by-slice procedure). The case of thin-walled pieces or large pieces susceptible to distortion is even more critical because of several factors that influence the distortion [13]. Therefore, tests on samples not used in practice are required. However, these tests are very time and material consuming. This is where simulations can help to reduce the uncertainties, costs, and time of the tests. Nevertheless, correlations have to be established between these simulated results and real cases. Therefore, the FEM approach could help in assessing residual stresses on large aluminum blocks. The method is being evaluated in large steel blocks by Sadheghifar et al. [14]. They demonstrated that an extended 3D FEM model could be used in DEFORM@software, version 11.0, to simulate the surface residual stresses on milled large blocks of steel [14]. The prediction of residual stresses does not come without challenges. In order to forecast the values and the distribution of residual stresses, it is important to know the material parameters (type, shape, and properties), the more appropriate material behavior models, friction models, the thermodynamics involved in processes, tool parameters, and the machining environment (dry, fluid, and with or without particles). From the cutting operation to the stress relaxation, the remaining stress in the material can be evaluated, as illustrated in Figure 1. When some of those parameters are well selected, compressive residual stresses can be promoted. Furthermore, researchers [15–18] have recently proposed post machining treatments of the workpiece as a workable solution to reduce residual stresses and improve the overall performance of the machined parts.

**Figure 1.** Residual stresses extraction steps.

Orthogonal cutting is widely used for simulating the machining processes [1,10,11,19–21]. The use of Finite Element methods (FEM) helps assessing responses that are difficult to measure and reduces expensive experimental tests. Two dimensions (2D) FEM technique was used by Javidikia et al. [5] to simulate the impact of edge radius, cutting speed, feed rate, and rake angle on the machining forces, cutting temperature, and chip thickness in dry turning of AA6061-T6. As indicated in their results, the machining forces and tool tip temperature were proportional to the cutting-edge radius and inversely proportional to the rake angle. Nonetheless, the variation of the edge radius showed little influence on the maximum temperature. However, the effect of tool geometry on residual stresses was not discussed. Tagiuri et al. [21] developed an FE model to predict the effect of the tool nose radius (10 to 900  $\mu\text{m}$ ), rake angle ( $-5^\circ$  to  $+10^\circ$ ), feed rate, and cutting speed on the cutting temperature, effective stresses, cutting forces, and tool wear during dry turning of AISI 1045 steel. Their results showed that for a certain nose range, a linear proportionality was proved between the cutting temperature and stresses. In addition, sharp tools (radii smaller or equal to 50  $\mu\text{m}$ ) slightly affected the cutting forces. However, further studies involving residual stresses could have been taken into consideration to have a better appreciation of the surface quality of the machined part.

Navas et al. [22] carried out an experimental study of the dry turning of AISI 4340 steel to evaluate the impact of the cutting speed, tool nose radius (0.4 and 0.8  $\mu\text{m}$ ), tool chip breaker geometry, and tool coating on surface residual stresses. They found that the surface residual stresses decreased with a smaller range of tool nose radii. However, the influence of the rake angle on the residual stresses distribution was not studied. Özel et al. [23] numerically and experimentally investigated the influence of different coated and uncoated carbide tools edge radii (5, 10, and 25  $\mu\text{m}$ ) on the forces and residual stresses during dry turning of Ti-6Al-4V and IN100 alloys. Their results shown indicated that augmenting the tool edge radius led to high forces and high compressive residual stresses in the material's depth but higher tensile residual stresses at the material's surface. However, the effect of the rake and clearance angle was not discussed.

Dry orthogonal cutting study was conducted by Jomaa et al. [24] to observe the impact of the cutting speed and feed rate on residual stresses during orthogonal turning of AA7075-T651. They observed that the impact of cutting speed on residual stresses was greater when smaller feed rates were used. However, the effect of the tool edge radius was not considered in this research study. Daoud et al. [10] studied the effect of rake angles ( $-8^\circ$ ,  $0^\circ$ , and  $+8^\circ$ ) on cutting forces, induced by dry orthogonal cutting of Al2024-T3. They also used DEFORM<sup>TM</sup>-2D software (version 8.1) to simulate the above machining responses. Their results demonstrated that by varying the rake angles from  $-8^\circ$  to  $+8^\circ$ , the cutting forces dropped by more than 50%. However, it was important to estimate the effect of the rake angle on the temperature distribution and residual stresses. Cheng et al. [25] developed a 2D FE model using AdvantEdge software (version 6.4) to predict the effect of the cutting tool rake angles and edge radii on temperature and tool stresses and optimize the above-mentioned parameters in orthogonal machining of Fe-Cr-Ni stainless steel. They reported that the cutting temperature was slightly affected by the edge radius. The tool stresses were minimized when the rake angle increased from  $0^\circ$  to  $10^\circ$  and the edge radius augmented from 40 to 80  $\mu\text{m}$ . The results also showed that the optimum values of the rake angle and edge radius were  $6^\circ$  and 60  $\mu\text{m}$ , respectively. However, the effects of the tool geometry parameters on the residual stresses in the machined workpiece were not predicted. Reddy et al. [26] utilized FE simulations to develop mathematical models of cutting forces and temperatures with respect to the cutting speed, feed rate, depth of cut, and tool edge radius during the dry turning of Ti-6Al-4V. They found that the feed rate and tool edge radius significantly affected cutting forces and temperatures. However, the impacts of the rake angle and angles were not investigated. This requires them to be studied in detail, which is thus the purpose of this article.

Liu and Xu [27] conducted experimental studies to analyze the impact of tool geometry on temperatures, forces, equivalent plastic strains, and residual stresses induced by orthog-

onal cutting of Inconel 718 alloy. They also used FE with the Coupled Eulerian–Lagrangian (CEL) technique with Abaqus/Explicit 6.4 software to predict those responses. Their observations revealed that a sharp edge radius tool with a negative rake angle produced more compressive stresses on the machined surface. However, obtaining the same behavior with AA6061-T6 is not certain.

A numerical method using Abaqus<sup>®</sup> was developed by Patel et al. [9] to numerically investigate the effect of the depth of the cut and rake angle on cutting forces during orthogonal machining of AA2024-T351. They found that the average cutting force and temperature were inversely proportional to the rake angle. However, their influence on the residual stresses was not discussed. Salman et al. [28] ran numerical and experimental tests to investigate the effect of the cutting speed, depth of cut, feed rate, tool (coated and uncoated), and tool nose radius (397, 794, and 1191  $\mu\text{m}$ ) on the cutting forces, maximum cutting temperature, and surface residual stresses in dry turning of AISI 1035 steel. Their simulations were conducted with AdvantEdge<sup>™</sup> software. They found that increasing the tool nose radius led to an increase in the mean temperature and created high tensile residual stresses. However, the impact of the tool rake and clearance angles on residual stresses were not examined. Moreover, the behavior of the residual stresses in the material's depth has not been discussed.

Javidikia et al. [3] conducted experimental and 2D simulation studies to investigate the effect of low-speed machining (LSM) and high-speed machining on tool forces and residual stresses under dry, MQL, and wet environments. Their results demonstrated that the feed rate has a much higher influence on the residual stresses compared to the cutting speed. However, the effect of tool geometry should have been considered to see how they interact with the cutting parameters.

Li and Chang [29] numerically investigated the effect of the tool cutting-edge radius on cutting force and stress concentration during machining of a nickel-based superalloy. The tool nose radii were varied between 0 and 85  $\mu\text{m}$ . They found that the Von Mises stresses on the workpiece and the cutting forces increased when using large tool nose radii, but the cutting shear angle decreased. However, the surface integrity was not studied. Rao et al. [30] worked on the residual stresses by varying the cutting speed and the feed rate. They obtained tensile residual stresses which are not advantageous for the material tool life, hence the need to consider the tool geometry parameters.

Despite FE having been applied, there are still many missing points that need to be investigated. From the above literature review, it can be depicted that there is limited research on the effect of tool geometry (edge radius, rake angle, and clearance angles) on cutting forces, cutting temperature, workpiece temperature, effective strain, effective stresses, and residual stresses in the literature. Such research works will help to better understand the essence of induced tensile and compressive residual stresses in the machined parts. Adding to that, the trend of residual stresses in the material's depth lack agreement in the literature and so these numerical studies will be a good contribution to the available research works.

## 2. Materials and Methods

In the present study, the orthogonal cutting process of AA6061-T6 is simulated by employing DEFORM<sup>™</sup> software (version 10.2) Among the other advantages of this software is the Lagrangian formulation, wherein the implicit integration method in the mathematical equations is used to perform and analyze large plastic deformations stimulated by the cutting process. The implicit solution is used to handle the convergence problem in every time increment. The implicit solution offers more stability than the explicit for small time increments. As a global equilibrium must be reached (solution must converge) before any state variable (stress, forces, temperature, etc.) is calculated, it is then easier to control the evolution of the solution at every step. More feedback is received as well as the number of

times increments. The tool's motion at a specific time given in Equation (1) can be increased gradually to prolong the analysis [5]:

$$[M]\{\ddot{U}\} = \{F_{ext}\} - \{F_{int}\} \quad (1)$$

$$\{F_{int}\} = [C_d]\{\dot{U}\} + [K_s]\{U\} \quad (2)$$

where  $[M]$ ,  $\{\ddot{U}\}$ ,  $\{F_{int}\}$ , and  $\{F_{ext}\}$  represent the mass matrix, acceleration vector, and internal and external vector forces, respectively. Similarly, the terms  $\{\dot{U}\}$  and  $\{U\}$  represent the velocity and displacement vectors.

The damping and stiffness matrices are written down by  $[C_d]$  and  $[K_s]$ , respectively. However, the effect of damping was ignored, because it is considered that there is no elastic drawback during cutting. In other terms, the object is permanently deformed (plastic deformation) after the yield strength is reached [5], i.e.:

$$[C_d] \cong 0 \quad (3)$$

Hence, Equation (2) becomes:

$$\{F_{int}\} \cong [K_s]\{U\} \quad (4)$$

### 2.1. Energy/Thermal Model

The total energy released during the cutting process can be defined by Equation (5) [5]:

$$[C_T]\{\dot{T}\} + [K_T]\{T\} = \{\dot{Q}_g\} \quad (5)$$

where  $[C_T]$  is the volumetric heat capacitance,  $[K_T]$  is the thermal conduction matrices, and  $\{\dot{Q}_g\}$  stands for the overall heat generation.

The energy exchanged between the tool and workpiece during thermal contact (heat of conduction) is expressed in Equation (6):

$$Q_{cond} = h_{int}(T_{wp} - T_t) \quad (6)$$

in which  $h_{int}$  is the heat transfer coefficient of conduction between the tool and workpiece,  $T_{wp}$  is the workpiece,  $T_t$  is the tool's temperature at the tool–chip interface, and  $Q_{cond}$  is the conductive heat transfer from the chip to the tool's face during the turning process.

The convection heat transfer occurs between the ambient air and the workpiece surface and can be calculated using Equation (7):

$$Q_{conv} = h(T_{wp} - T_a) \quad (7)$$

where  $h$  is the heat transfer coefficient of convection and  $T_a$  is the ambient temperature.

In our simulations, a heat transfer coefficient of  $10^7 \text{ W/m}^2 \text{ }^\circ\text{C}$  was used, and the room temperature was taken at  $20 \text{ }^\circ\text{C}$  for both the tool and workpiece [3].  $Q_{conv}$  is the convective heat transfer from the chip, tool, and workpiece with the environment.

In this study, the heat transfer coefficient was calibrated when the steady-state condition for the cutting temperature was reached. The high value was selected because the high pressure of the chip on the tool rake face makes perfect contact between the tool and the chip [31]. Another reason was to quickly reach the steady-state condition in order to shorten the cutting time and avoid excessive distortion of the elements [31]. Most importantly, this high value provided good agreement between the experiments and predictions.

## 2.2. Workpiece and Tool Geometry, Mesh, and Properties

In the numerical setup, an elastic–plastic body type was considered for a 4.8 mm × 1.12 mm × 4 mm workpiece which was meshed with at least 3000 elements and 3000 nodes. A rigid body type was attributed to the tool material, which was meshed with a minimum of 1800 elements and 1800 nodes. The width of cut was set to 4 mm. An illustration of the workpiece and tool (geometry and dimension) is shown in Figure 2 where the objects and generated meshes are represented. DEFORM™ software uses the automatic remeshing method, in which new mesh is generated when mesh distortion is detected [8,31]. In this research work, the workpiece was meshed with at least 3000 linear quadrilateral elements and 3000 nodes. The tool material was considered as a rigid body and was meshed with 1800 elements and 1800 nodes. Mesh windows were assigned to the tool tip and part of the rake and flank faces in order to have a high-quality fine mesh in the cutting zone. Mesh windows were also assigned to the workpiece to have a high-quality fine mesh in the machined workpiece to accurately predict and extract the superficial residual stresses with a reduced CPU time [8]. An interference depth of about 0.00195 mm was used to start a remeshing procedure for the workpiece. The mechanical and thermal properties of the workpiece and tool materials are shown in Table 2.

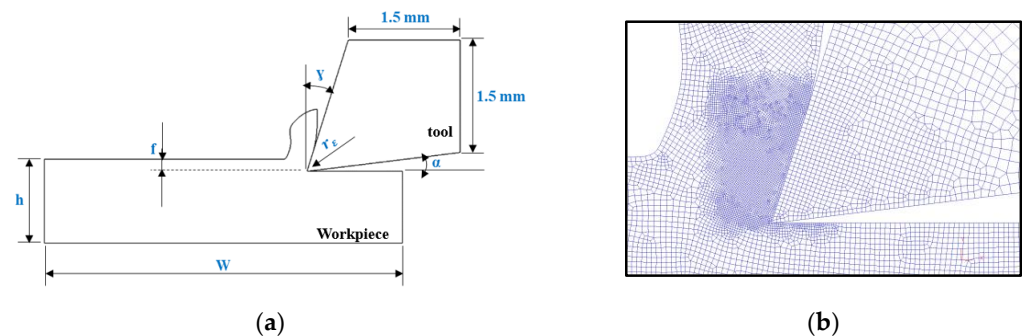


**Figure 2.** (a) Workpiece and tool geometry and (b) Mesh generation.

**Table 2.** Mechanical and thermal properties of the workpiece and tool (reprinted with permission from [5], 2023, Licence No 5513161238525, Springer nature).

Properties	AA6061-T6	Uncoated Carbide
Density $\rho$ (kg/m <sup>3</sup> )	2700	11,900
Young's modulus $E$ (GPa)	58.5	650
Poisson's ratio $\nu$	0.33	0.25
Conductivity $k$ (W/m°C)	167	59
Specific heat capacity $c$ (J/kg°C)	896	337
Thermal expansion coefficient $\alpha$ (1/°C)	$23.5 \times 10^{-6}$	$5 \times 10^{-6}$

The cutting conditions and tool geometry parameters used in this study are shown in Table 3. These parameters are an extension of published models in the literature [3,5]. High speed machining was found by the authors to give better results in terms of the forces and stresses. Hence, it was used in our study. In all the simulated tests, the cutting speed is kept constant at 950 m/mins and the feed rate at 0.16 mm/rev.

**Table 3.** Cutting conditions and tool geometry parameters.

Cutting Speed $V_C$ (m/min)	Feed Rate $f$ (mm/rev)	Tool Edge Radius $r_\beta$ ( $\mu$ m)	Rake Angle $\gamma_o$ (°)	Clearance Angle $\alpha_o$ (°)
950	0.16	5; 10; 20; 40	−8; 8; 17.5; 20	2; 7; 11; 17.5

### 2.3. The Material Model, Boundary Conditions, and The Friction Model

#### 2.3.1. Material Model

The turning process usually involves large thermal, plastic, and strain deformations. To ensure the continuity of the workpiece material flow during this process, the Johnson–Cook constitutive Equation (8) was used:

$$\sigma_{fl} = [A + B\varepsilon^n] \left[ 1 + C \ln \left( \frac{\dot{\varepsilon}}{\dot{\varepsilon}_0} \right) \right] \left[ 1 - \left( \frac{T - T_{room}}{T_{melt} - T_{room}} \right)^m \right] \quad (8)$$

where  $\sigma_{fl}$  is the flow stresses of the workpiece material,  $A$  is the initial yield strength,  $B$  is the hardening modulus,  $C$  is the strain rate sensitivity coefficient,  $n$  is the hardening coefficient, and  $m$  is the thermal softening coefficient. The plastic strain, plastic strain rate, and reference plastic strain rate are represented by  $\varepsilon$ ,  $\dot{\varepsilon}$ , and  $\dot{\varepsilon}_0$ , respectively.  $T$ ,  $T_{melt}$ , and  $T_{room}$  represent the workpiece and melting and room temperatures, respectively. The Johnson–Cook constants of AA6061-T6 are shown in Table 4. The failure/damage model was not employed in this research study since continuous chip formation (not segmented) was assumed for all the simulations. This assumption can be justified based on the observations of chips for all the selected cutting conditions reported by [5,8].

**Table 4.** Johnson–Cook material model’s constants of the of AA6061-T6 (reprinted with permission from [5], 2023, Licence No 5513161238525, Springer nature).

A (MPa)	B (MPa)	$n$	$C$	$m$	$\dot{\varepsilon}_0$ (1/s)	$T_{melt}$ (°C)	$T_{room}$ (°C)
250	79.70	0.499	0.0249	1.499	1	652	20

#### 2.3.2. Boundary Conditions

The geometry and boundary conditions (BCs) of both the workpiece and tool are shown in Figure 3a. In DEFORM<sup>TM</sup> 10.2, it was assumed that the workpiece moved uniformly along the horizontal x-direction ( $V_x = V_c = \text{constant}$  and  $V_y = 0$ ), across a fixed tool. This last condition was kept fixed on both vertical and horizontal directions ( $V_x = 0$  and  $V_y = 0$ ).

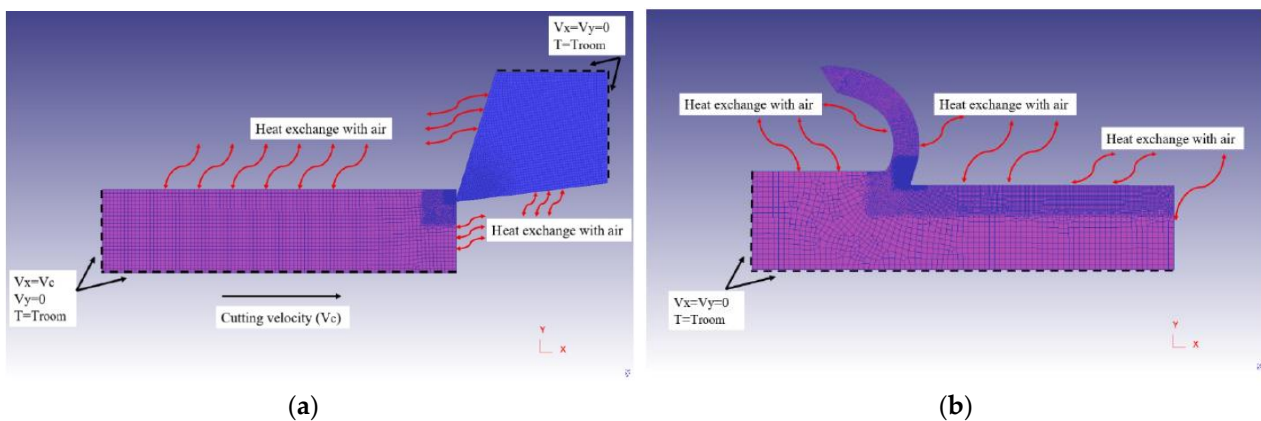


**Figure 3.** BCs in DEFORM<sup>TM</sup> [3]. (a) For the elasto–plasto cutting model and (b) BCs for the residual stresses model.

Both sides of the workpiece and tool were kept away from the cutting zone and exposed to the atmosphere, where the air temperature was set as  $T_{room} = 20$  °C. Figure 3b shows the BCs for the residual stresses’ calculations, whereby the tool is removed from the workpiece surface and the workpiece allowed to cool down to approximately the room temperature. The procedure is detailed in the residual stress model (Section 2.3.4).

### 2.3.3. Friction Model

The available literature shows that a built-up layer can take place at the tool's rake face during the machining of aluminum alloy. This is due to the high force and temperature at the tool–chip interface. In addition, the ductile nature of aluminum contributes to the melting of some parts of the material as it flows along the tool's rake face. As investigated by Javidikia et al. [3], the Coulomb model does not offer relative sliding at the tool–chip interface. Hence, the shear model was used in our simulations to model the frictional forces at the tool–workpiece–chip interfaces. The shear stress ( $\tau$ ) on the rake face of the tool were calculated using the formula in Equation (9):

$$\tau = 0.98 \tau_{Chip} \quad (9)$$

where  $\tau_{Chip}$  is the shear flow stress in the chip at the tool–chip interface.

### 2.3.4. The Residual Stress Model

Once the cutting simulation was completed and the solution had reached a steady state, the next step consisted of extracting the stresses that remained on the workpiece material after a stress–relaxation process. This ensured that the residual stresses are unbalanced in the workpiece. During this process, the tool was removed and re-positioned far away from the workpiece (as seen in Figure 2b.), and only a convective heat transfer operation was affected on the workpiece. This allowed the workpiece to relax and cool down to a temperature standing between 20–50 °C [3]. In DEFORM, some steps were taken to find the residual stresses in the machined parts.

## 3. Results and Discussion

The effect of tool geometry parameters, including the tool edge radius, rake angle, and clearance angle, on cutting temperature, forces, and residual stresses induced by dry orthogonal cutting of AA6061-T6 was studied and presented in the next sections.

### 3.1. Effect of the Tool Edge Radius

#### 3.1.1. Effect of the Tool Edge Radius on the Cutting Forces and Temperatures

Different edge radii (5, 10, 20, 30, and 40  $\mu\text{m}$ ) are used in this study. The dynamics force distribution along the cutting time is shown in Figure 4. In Figure 4, it is observed that at the beginning of the cutting process, both the cutting and thrust forces increase from zero to their maximum and then fluctuate (sinusoidal trend) between a maximum and minimum value. After some time, the forces keep their stability. This state is called the steady state when they have reached their equilibrium, and the curve “appears” to be linear. The average value of the forces can be calculated by averaging the values at the steady line and the overall maximum or minimum of the forces can also be found. At the steady state, all the other variables (stresses, temperature, pressure, etc.) reach their equilibrium and righter solutions are obtained.

On Figure 4, a high increase in the first load is observed as an elastic–plastic model used. The model first starts to deform elastically. Once the yield stress is reached, the material starts to then deform plastically. The cutting and thrust forces increase gradually as the radius increases. Some drop down (breakage) zones are observed. These are caused by the outlier points recorded during the continuous cutting time. However, they can be explained by the fact that when the load is high, there are many workpiece nodes in contact with the tool nodes. A constant shear friction factor of 0.98 is considered. This means the resistance to sliding for all slave (workpiece) nodes sliding on the master (tool) surface will be multiplied by the flow stress. When the contact is finally lost, the workpiece springs away from the tool and much fewer nodes are in contact and the temperature drops. Hence, much less resistance to sliding is encountered and a drop in the load is observed. The small “chatter” noise in the plots is likely due to nodes moving along the surface and leaving and contacting the surface. The workpiece is discretized into elements with nodes. When a

node leaves the surface of the tool, there may be a sudden drop in contact area and thus frictional load.

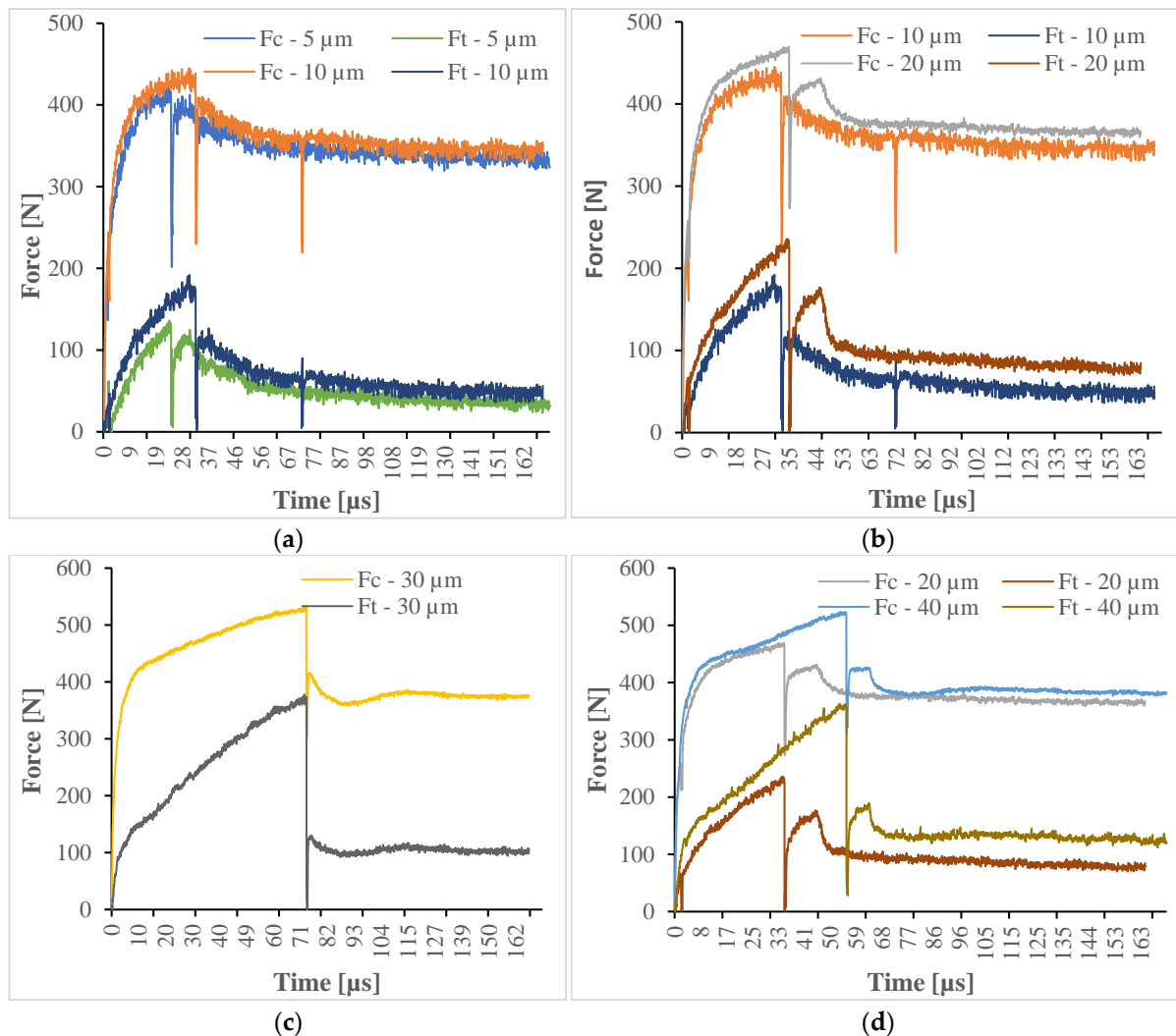


**Figure 4.** Force distribution during cutting process for different - edge radius ( $\alpha = 7^\circ$  and  $\gamma = 17.5^\circ$ ): (a) 5–10  $\mu\text{m}$ , (b) 10–20  $\mu\text{m}$ , (c) 30  $\mu\text{m}$ , and (d) 30–40  $\mu\text{m}$ .

The influence of the tool edge radius on the cutting temperature, forces, and residual stresses were studied. The edge radii varied from 5  $\mu\text{m}$  to 40  $\mu\text{m}$ , and the tool temperature distribution along the tool rake face is shown in Figure 5. There, the relationships between the edge radius, forces, and largest tool tip temperature with associated forces trend during machining are presented. These figures show that the maximum tool tip temperature is proportional to the edge radius. The increase in temperature is caused by the growth of the contact area around the tip of the tool, generated by the increase in tool tip temperature as observed in Figure 5. This would require a larger ploughing force and specific energy, which would produce more heat at the primary and secondary cutting zones. Figure 6 illustrates the variation on the largest tool tip and rake face temperatures as well the cutting forces behavior varying along with the edge radius. Figure 6 shows that the forces and temperature are both proportional to the edge radius. It is noticed that the temperature at the tool's rake face increases slightly compared to the tool tip temperature, since the tool's tip is very near the edge radius. Here again, the direct relationship between forces and temperatures can be noted. Comparable results were found by Yen et al. [32]. They saw that increasing the edge radius from 0.01 to 0.1 mm caused an increase in the cutting forces and temperature. Javidikia et al. [5] and Tagiuri et al. [21] made similar conclusions.

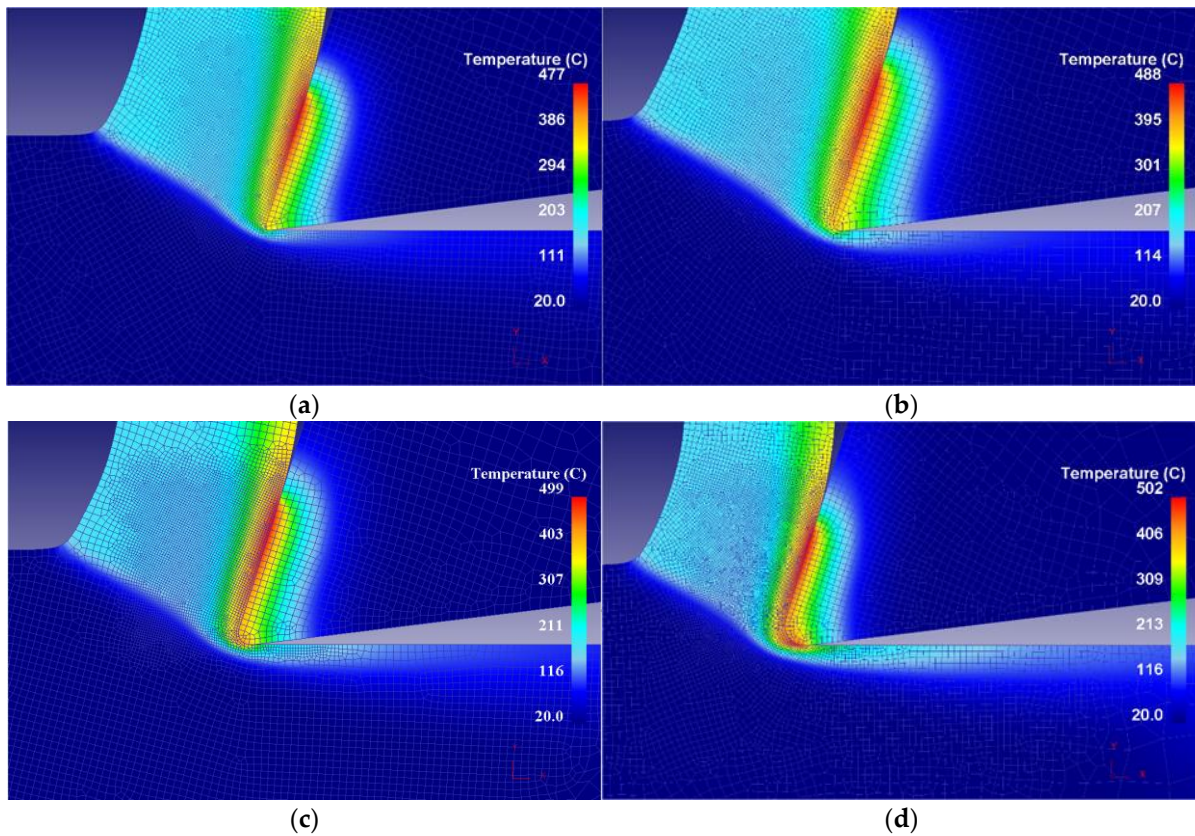


Figure 5. The distribution of cutting temperature in DEFORM™ at various edge radius for.  $\alpha = 7^\circ$ ,  $\gamma = 17.5^\circ$ : (a) 5  $\mu\text{m}$ , (b) 10  $\mu\text{m}$ , (c) 20  $\mu\text{m}$ , and (d) 40  $\mu\text{m}$ .

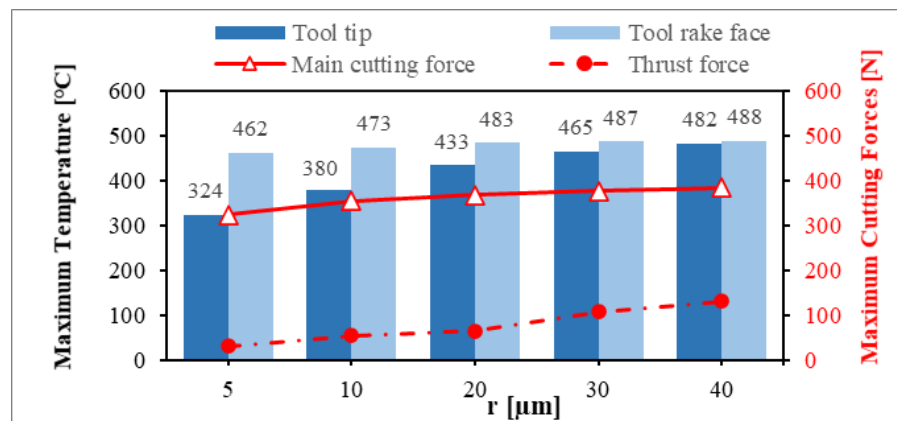
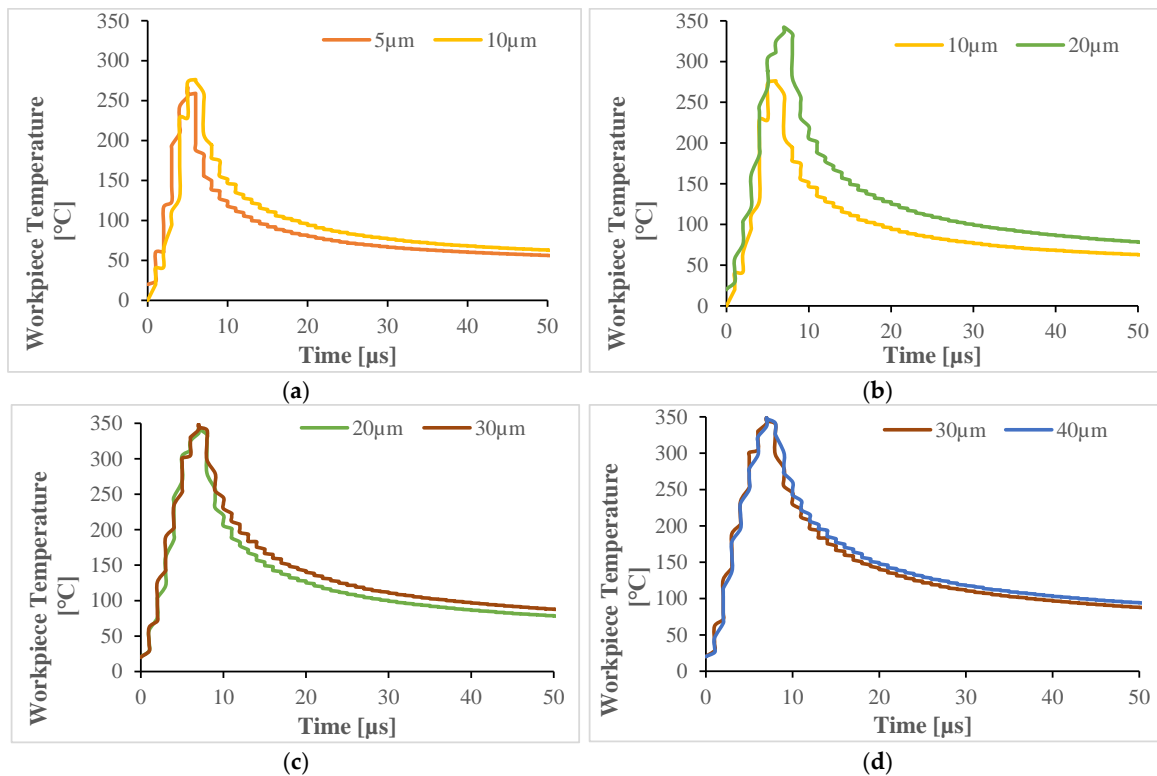


Figure 6. Relationship between the edge radius, forces, and maximum temperature.

The instantaneous workpiece temperature results for 5 to 40  $\mu\text{m}$  radius are shown in Figure 7. The results were obtained by tracking a fixed point P1 on the workpiece from the start until the end of the cutting process. It is observed that the temperature increases suddenly a few seconds after the first steps. This is explained by the sudden rise of the cutting forces in Figure 4. The maximum temperature occurs at the tool–workpiece interface where the friction between the workpiece and tool is high. Then, after the temperature drops and reaches a steady-state condition, all the variables can be measured with more accuracy. From 5 to 40  $\mu\text{m}$ , the instantaneous workpiece temperature seems to increase with the edge radius. The highest temperature of the workpiece is reached at 40  $\mu\text{m}$  and the lowest is observed at 5  $\mu\text{m}$ . These results are the consequences of temperature and forces behavior discussed in Figures 4–6.



**Figure 7.** Workpiece surface temperature respect to the edge radius ( $\alpha = 7^\circ$  and  $\gamma = 17.5^\circ$ ): (a) 5–10  $\mu\text{m}$ , (b) 10–20  $\mu\text{m}$ , (c) 20–30  $\mu\text{m}$ , and (d) 30–40  $\mu\text{m}$ .

The variation of the forces and temperature have been discussed. However, it is acceptable to go back and understand the results obtained in the earlier sections. Hence, analyzing the deformation and stresses behavior on the workpiece during cutting is a good starting point. The largest instantaneous workpiece temperatures are extracted from Figure 6 and the relationship with strain and stress can be drawn from Figure 8. From 5 to 10  $\mu\text{m}$ , a slight variation of the temperature is clearly seen. The deformation (strain) in the machined workpiece sits between 0 and 0.8 mm/mm. Overall, as the workpiece temperature increases all along with the edge radius, the deformation increases along with the equivalent stresses. The regions of strain above 2 mm/mm and stresses above 200 MPa are marked by the strong concentration of the red color. It is then observed that at 40  $\mu\text{m}$  the deformation is more pronounced, as are the stresses. These results are justified by the results obtained for the high values of cutting temperature and forces at 40  $\mu\text{m}$ .

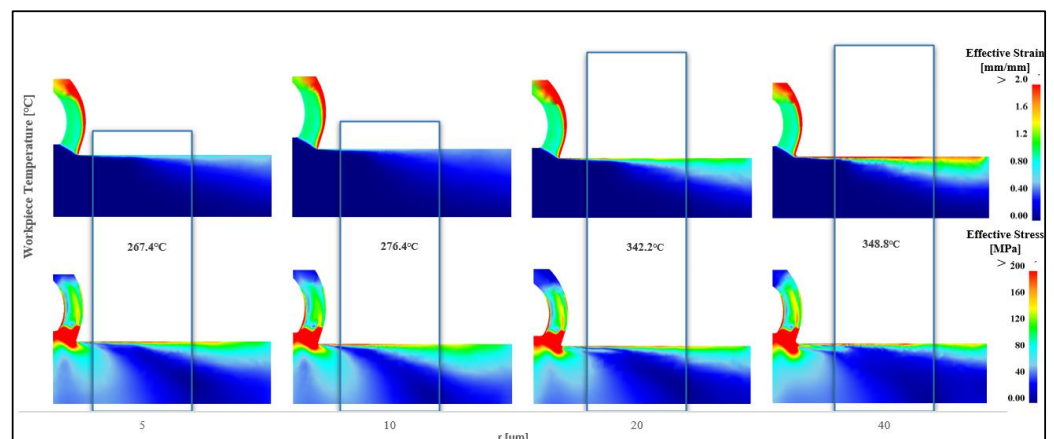


**Figure 8.** Maximum workpiece temperature–strain–stress simulations with respect to the edge radius.

### 3.1.2. Effect of the Edge Radius on Residual Stresses

The residual stresses at the surface and subsurface of the machined workpiece were calculated along the  $y$ -axis near the edge for various edge radii. The selected state variables were distributed among 40 points from the machined workpiece's surface until about 0.9 mm below the surface. These measurements were performed far from the shear zone at about 0.84 mm away from the start point, as shown in Figure 9.

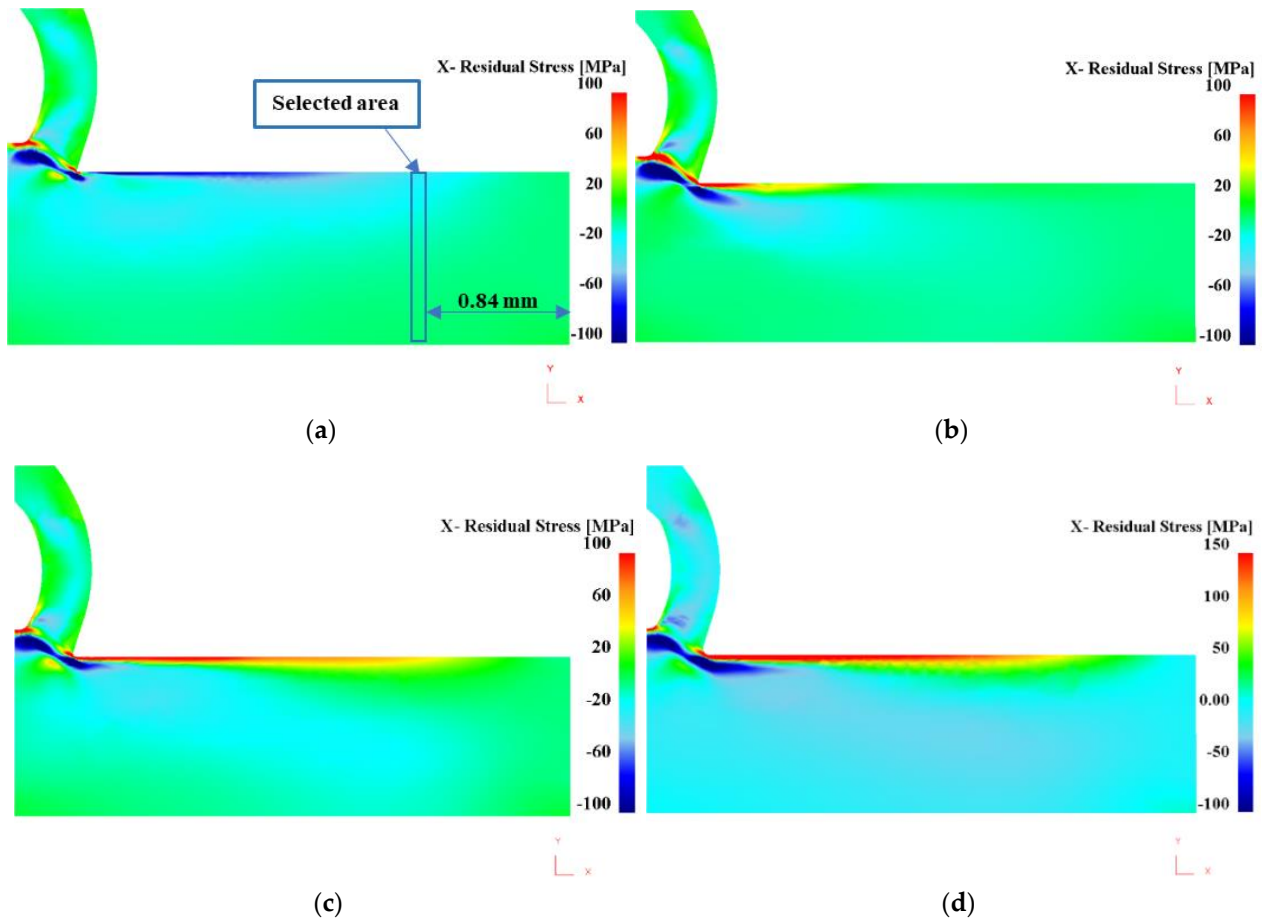


**Figure 9.** Residual stresses simulations with respect to the edge radius: (a) 5  $\mu\text{m}$ , (b) 10  $\mu\text{m}$ , (c) 20  $\mu\text{m}$ , and (d) 40  $\mu\text{m}$ .

According to Figure 9a–d, the residual stresses increased from compressive to tensile with increasing tool edge radius. The lowest value of tensile residual stresses at the surface is found to be 4.6 MPa for a 10  $\mu\text{m}$  edge radius. The highest tensile stresses occur at 40  $\mu\text{m}$  with a value of about 108.6 MPa. Compressive residual stresses exist for a 5  $\mu\text{m}$  edge radius. They are about  $-26.6 \mu\text{m}$  at the machined surface of the selected area. These results can be credited to the fact that an increasing tool edge radius increases the tool–chip–workpiece contact area and the frictional heat, leading to a higher cutting temperature, and resulting in larger residual stresses for an edge radius above 10  $\mu\text{m}$ . This result agrees with that obtained by Nasr et al. [19], who reported that the residual stresses increased with raising the tool edge radius in the orthogonal cutting of AISI 316L steel.

Thus, the tool edge radius of 5  $\mu\text{m}$  is suggested as capturing the lowest value of residual stresses. From the machined surface until beneath, the results show that residual stresses followed “tensile–compressive” or “compressive–tensile” behaviors. This leads us to predict the feed range, which in this case is the depth of the cut, that produces the compressive residual stresses. According to Figure 10, feed rates occur in the range of 0 to 0.4, 0.098 to 0.96, 0.24 to 0.96, 0.32 to 0.96, and 0.29 to 0.96 mm intervals and would generate compressive residual stresses for edge radii of 5, 10, 20, 30, and 40  $\mu\text{m}$ , respectively. Out

of this range, tensile residual stresses would be expected. Moreover, the residual stresses curves are observed to cross each other for the depth of cut including 0.2 and 0.4 mm for edge radii sitting below 30  $\mu\text{m}$  and comprised between 0.2 to 0.3 and for the edge radii greater than 30  $\mu\text{m}$  between 0.3 to 0.96 mm. This analysis can help to predict desirable residual stresses for a specific range of tool geometry. Lastly, it is observed that the zero residual stresses (location of the bulk material) are quickly reached for edge radius values (10, 20, and 30  $\mu\text{m}$ ). However, for the fine insert (5  $\mu\text{m}$ ) the bulk material appears at the bottom end of the workpiece. The behavior of the 30  $\mu\text{m}$  and 40  $\mu\text{m}$  radii in the machining responses are almost similar.

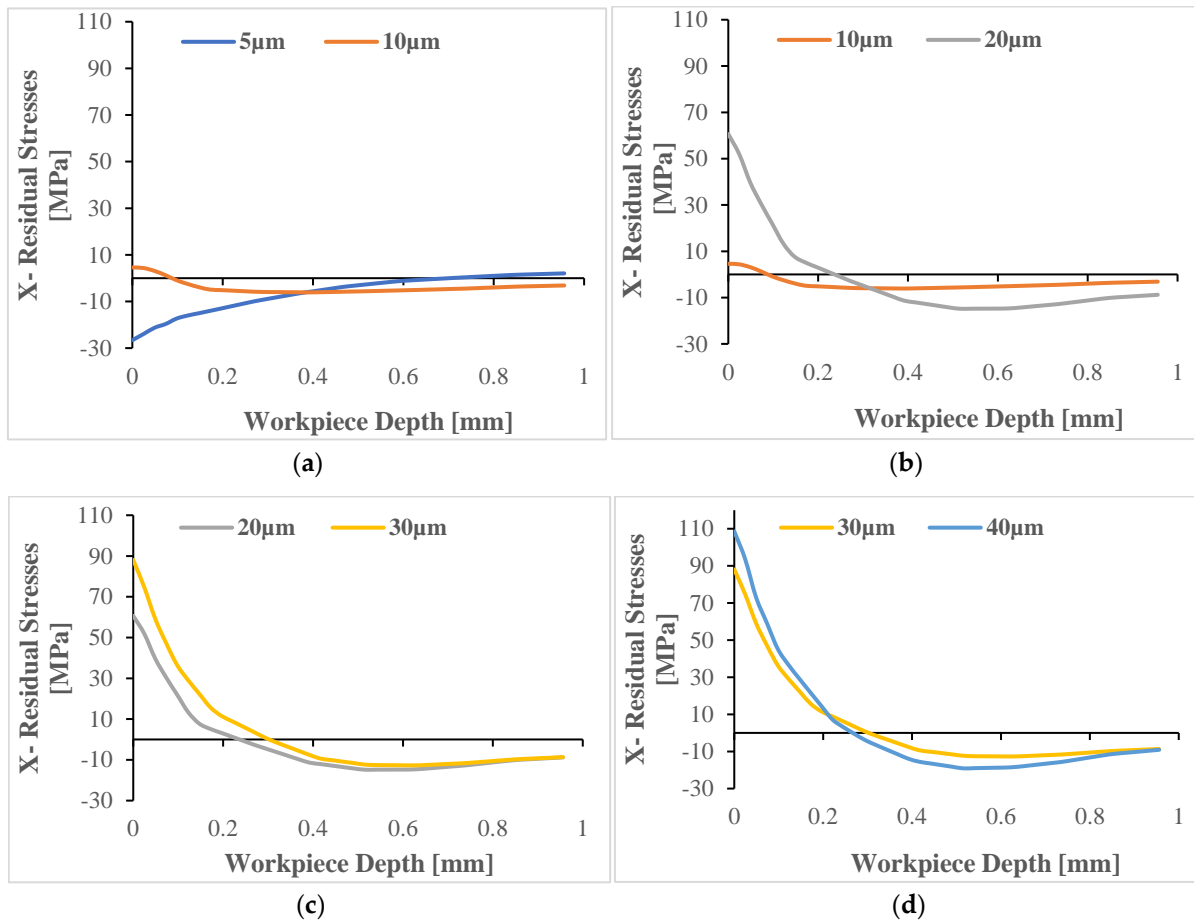


**Figure 10.** Effect of edge radii on residual stresses ( $\alpha = 7^\circ$  and  $\gamma = 17.5^\circ$ ). Workpiece and selected path, (a) 5–10  $\mu\text{m}$ , (b) 10–20  $\mu\text{m}$ , (c) 20–30  $\mu\text{m}$ , and (d) 30–40  $\mu\text{m}$ .

### 3.2. Effect of the Rake Angle

#### 3.2.1. Effect of the Rake Angle on the Cutting Forces and Temperature

Different rake angles including  $-8^\circ$ ,  $0^\circ$ ,  $+8^\circ$ , and  $+20^\circ$  are used in this study. The dynamics force distribution along the cutting time is shown in Figure 11. From the curves of main cutting forces ( $F_c$ ) and thrust forces ( $F_t$ ), the maximum cutting forces are inversely proportional to the rake angle and proportional for positive rake angles. This is for the rake angles lying in between  $-8^\circ$  and  $+8^\circ$ . From  $+8^\circ$  to  $20^\circ$ , the maximum cutting forces do not vary much as the rake angle increases. However, the thrust forces increase slightly. However, the average forces at the steady state positions decrease as the rake angle increases. Patel et al. [9] agreed with the same results.

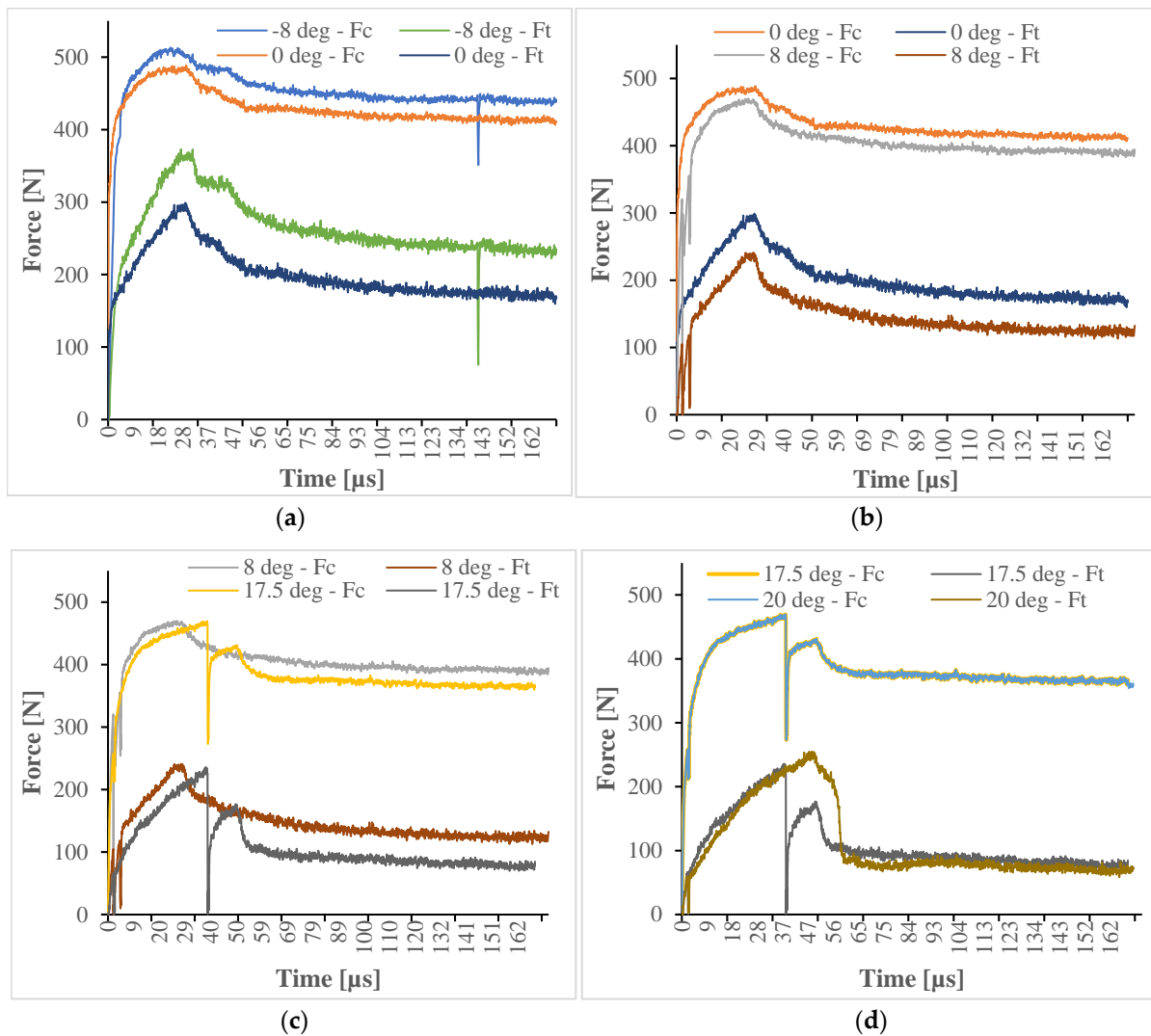


**Figure 11.** Force distribution during cutting process for different rake angles ( $\alpha = 7^\circ$  and  $r_e = 20 \mu\text{m}$ ): (a)  $-8-0^\circ$ , (b)  $0-8^\circ$ , (c)  $8-17.5^\circ$ , and (d)  $17.5-20^\circ$ .

The simulation results of the tool temperature are shown in Figure 12. It is clearly observed that the maximum tool temperature occurs at the rake face of the tool. As noted, the negative rake angle produces more heat which decreases while the values of the rake angle are augmented. Since the tool–chip contact area becomes much larger compared to the other cases where the angles are positive, more friction, meaning more resistant force, was needed to move the chip onto the tool rake face. These results agree with Daoud et al. [33] who proved that changing the rake angle from negative to positive values slightly decreases the amount of temperature at the tool–chip interface. Figure 13 illustrates the variation on the largest tool tip, rake face temperatures, and the cutting forces behavior as the rake angle differs.

Figure 13 shows that the forces and temperature are inversely proportional to the rake angle. This is shown by the negative slope obtained. Nonetheless, for the rake angle formed between  $17.5^\circ$  and  $20^\circ$ , the cutting forces and temperatures vary very slightly. Once again, the direct relationship between the forces and temperatures is noteworthy.

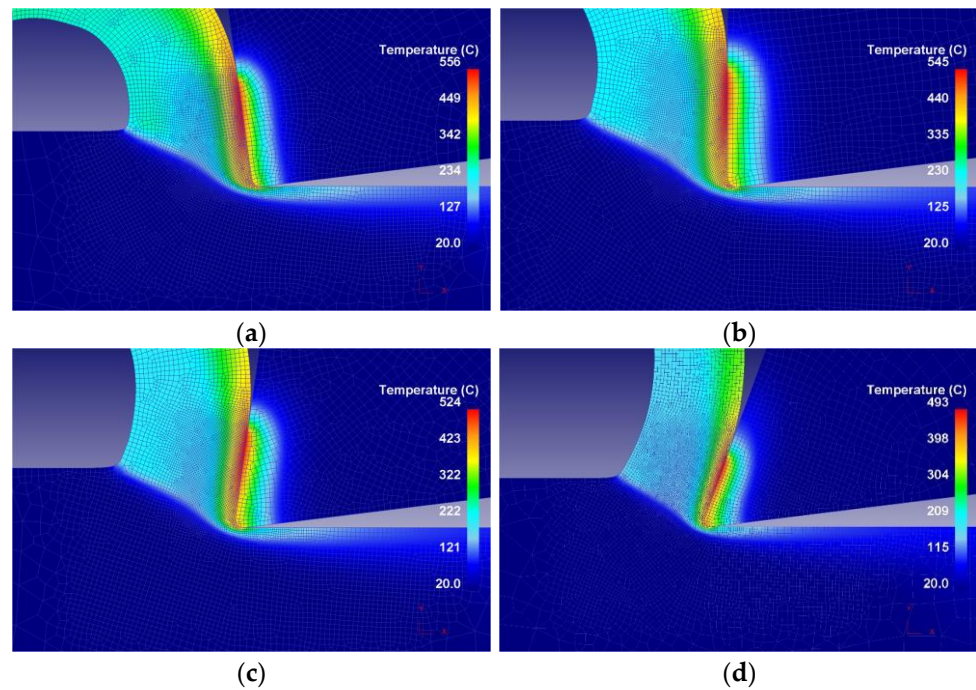


**Figure 12.** The distribution of cutting temperature in the machined surface for the rake angles ( $\alpha = 7^\circ$  and  $r_\epsilon = 20 \mu\text{m}$ ): (a)  $-8^\circ$ , (b)  $0^\circ$ , (c)  $+8^\circ$ , and (d)  $20^\circ$ .

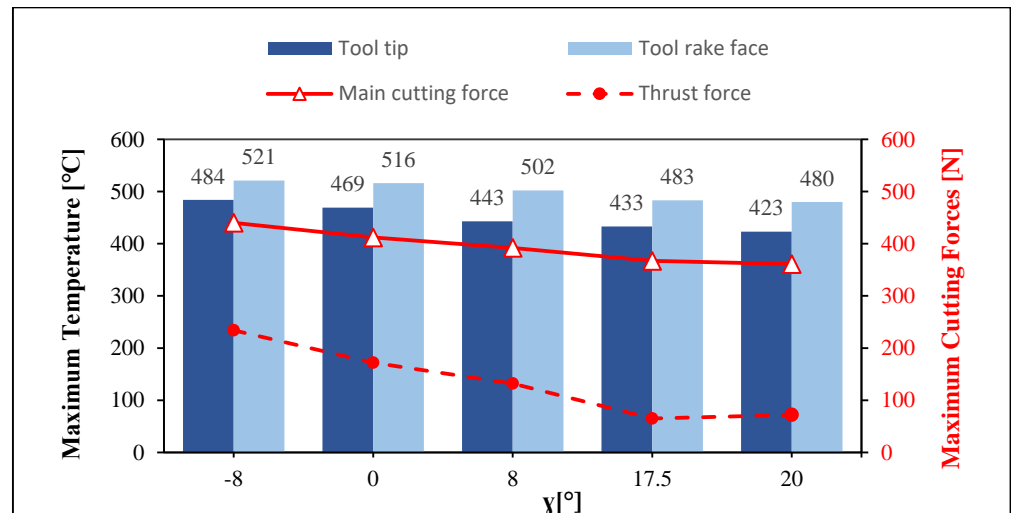


**Figure 13.** Relationship between the rake angle, force, and temperature.

The instantaneous workpiece temperature results from  $-8^\circ$  to  $20^\circ$  values of the rake angle are shown in Figure 14. The results were obtained by tracking a fixed point P1 on the workpiece from the start to the end of the cutting process.

In Figure 14, it is observed that the temperature rises suddenly and then drops until it reaches a steady state condition. At that condition, all the states variables can be measured with more accuracy. From negative rake angles, the workpiece temperature seems to decrease as the rake angle increases. As for the positive rake angle, from  $8^\circ$  above the proportionality between the workpiece temperature and the rake angle is observed. The highest temperature of the workpiece is reached at  $20^\circ$  and the lowest is observed at  $-8^\circ$ . There is not much variation in the workpiece temperature as the rake angle increased slightly ( $2.5^\circ$ ).

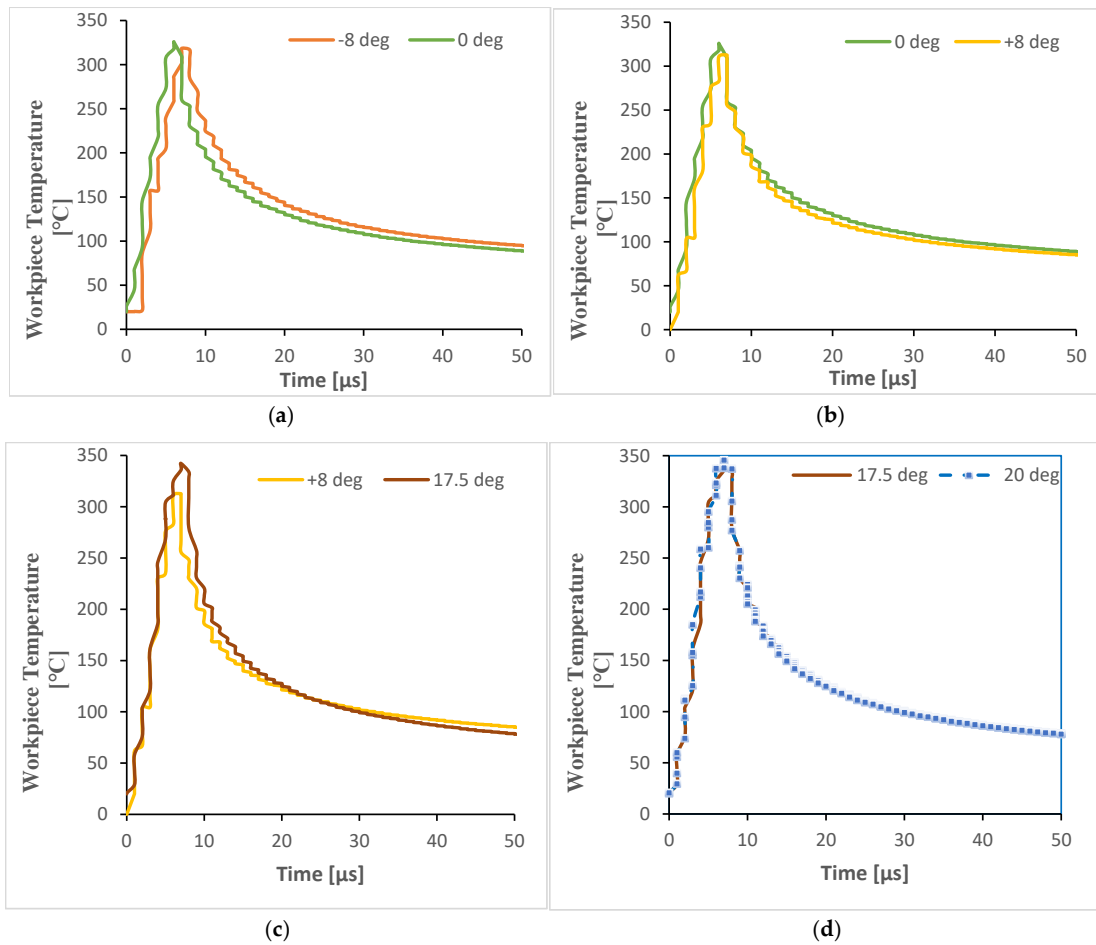


**Figure 14.** Effect of rake angle on Workpiece surface temperature ( $\alpha = 7^\circ$  and  $r_e = 20 \mu\text{m}$ ): (a)  $-8-0^\circ$ , (b)  $0-8^\circ$ , (c)  $8-17.5^\circ$ , and (d)  $17.5-20^\circ$ .

Figure 15 is the variation of strain and stress with the largest instantaneous workpiece temperatures with respect to the rake angle. In Figure 14 it is observed that the workpiece temperature increases slightly from  $-8^\circ$  to  $0^\circ$ . Then, from  $0^\circ$  to  $+8^\circ$ , the maximum temperature decreases slightly and changes quickly from  $8^\circ$  to  $17.5^\circ$ . However, the effective strain and stresses decrease as the rake angles increase.

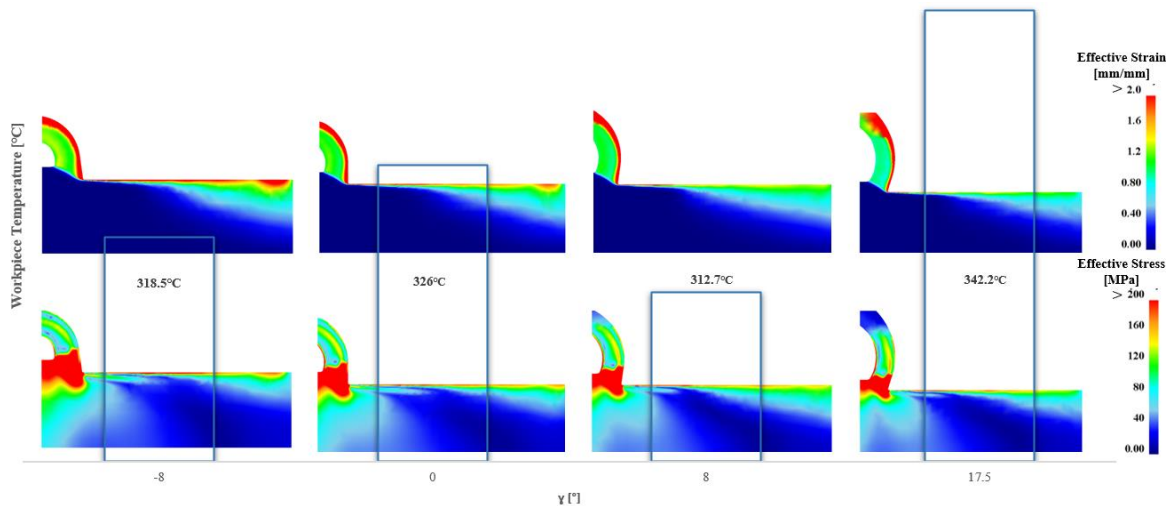


**Figure 15.** Maximum workpiece temperature–strain–stress simulations with respect to the rake angle.

### 3.2.2. Effect of the Edge Radius on Residual Stresses

The measurements of residual stresses were taken far from the shear zone at about 0.84 mm away from the starting point, as shown in Figure 16a. According to Figure 16a–d, the residual stresses increase from  $-8^\circ$  to  $0^\circ$  and decrease with an increasing rake angle from  $0^\circ$  to  $17.5^\circ$ . The effects of the rake angles observed can be explained by the decrease in temperature and forces due to the reduction in the contact area between the tool–chip interfaces (See Figure 13). It is known that a high negative rake angle leads to high tool–chip contact pressure, generating a high frictional heat and cutting temperature [34,35] resulting in high residual stresses. This is confirmed by [36] and [37], where residual stresses are augmented by reducing the rake angle from a positive to a negative direction.

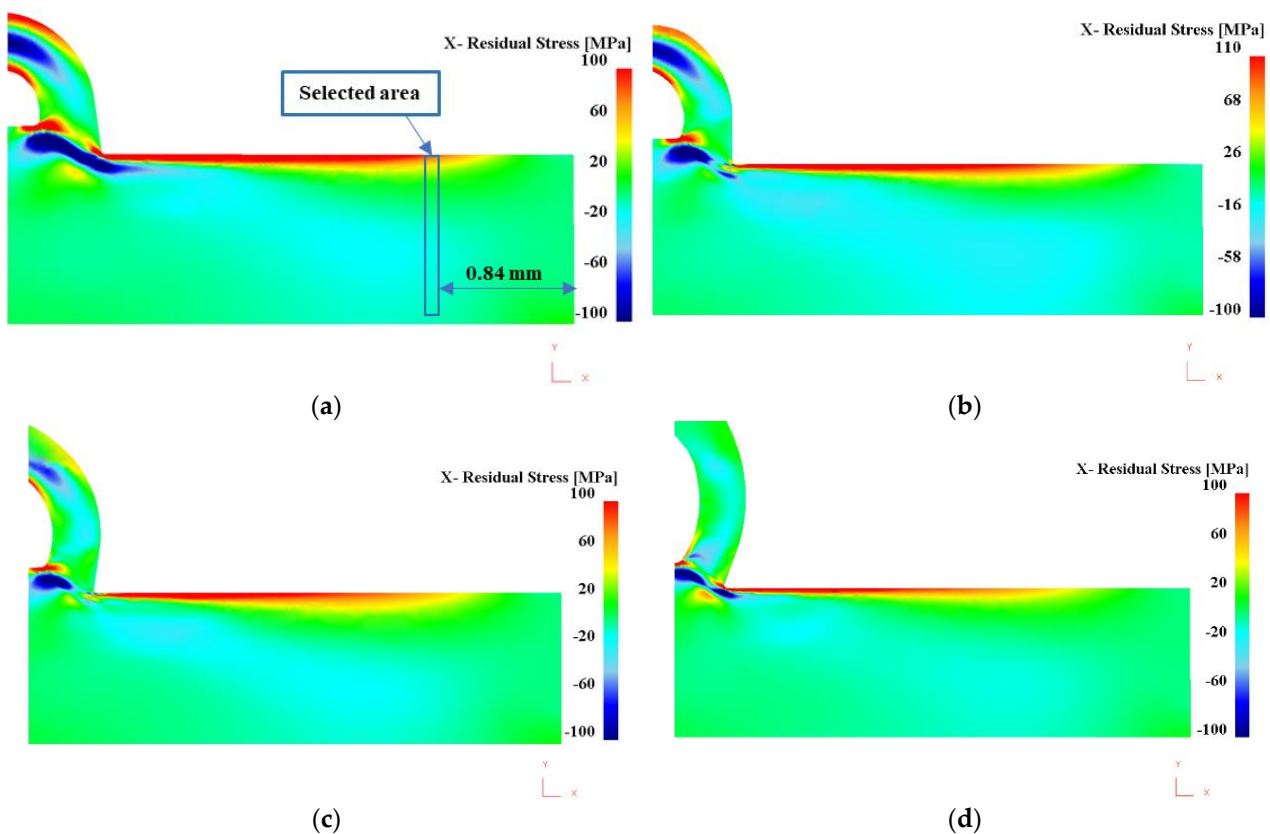


**Figure 16.** Simulation results of residual stresses along the workpiece's depth ( $\alpha = 7^\circ$  and  $r_\epsilon = 20 \mu\text{m}$ ): (a)  $-8^\circ$ , (b)  $0^\circ$ , (c)  $17.5^\circ$ , and (d)  $20^\circ$ .

The simulations result of the residual stresses on the rake angles are plotted in Figure 16. From there, tensile residual stresses are produced at the machined surface of the workpiece. It is observed that as the rake angle increases from  $-8$  to  $0^\circ$  the tensile residual stresses increase, but they decrease as the rake angle increases in the positive direction from  $0^\circ$  to  $17.5^\circ$ . Between  $17.5^\circ$  and  $20^\circ$ , the residual stresses do not vary much.

The lowest value of tensile residual stresses at the surface is found to be 60.64 MPa for a  $17.5^\circ$  rake angle value. The highest tensile stresses take place at  $0^\circ$  with a value of about 103.76 MPa. Beneath the machined surface, zero absolute residual stresses are obtained when the depth makes up between 0.2 and 0.4 mm. Below that range, compressive residual stresses are obtained. According to Figure 17, it can be drawn that a rake angle of  $17.5^\circ$  produces higher compressive stresses. However, the difference in the values of compressive residual stresses do not change much as the rake angles vary. These appearances of residual stresses are aligned with the results obtained by [29]. They examined the residual stresses produced during the machining of Inconel. They found that high tensile stresses were produced.

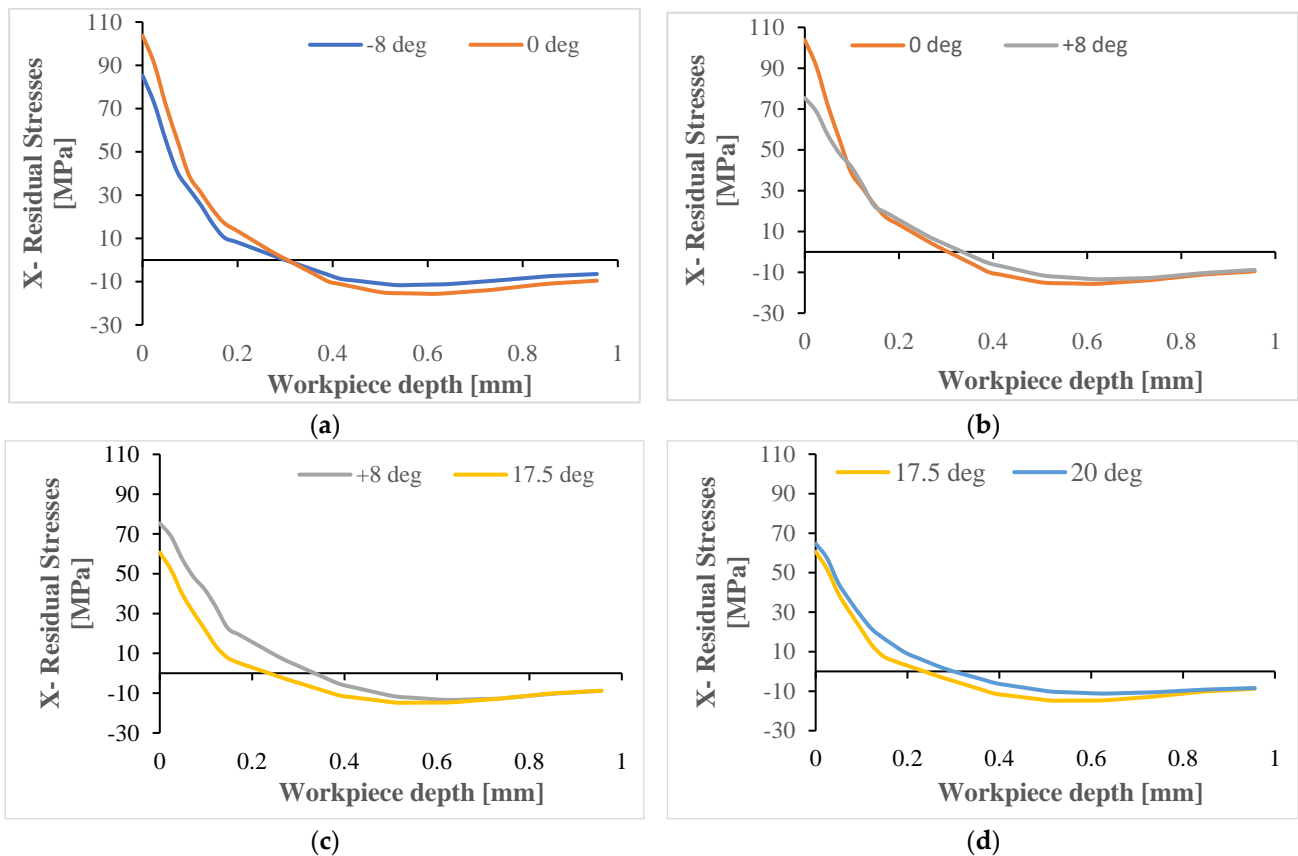


**Figure 17.** Residual stresses profile for various rake angles ( $\alpha = 7^\circ$  and  $r_\epsilon = 20 \mu\text{m}$ ): (a)  $-8^\circ$ , (b)  $0^\circ$ , (c)  $17.5^\circ$ , and (d)  $20^\circ$ .

### 3.3. Effect of Clearance Angle

#### 3.3.1. Effect of the Clearance Angle on the Cutting Forces and Workpiece Temperature

Different clearance angles including  $2^\circ$ ,  $7^\circ$ ,  $11^\circ$ , and  $17.5^\circ$  are used in this study. The dynamics force distribution along the cutting time is shown in Figure 18. From this figure, it is observed that as the clearance angle increases from  $2^\circ$  to  $17.5^\circ$ , the cutting forces decrease ever so slightly. Between  $11^\circ$  and  $17.5^\circ$  the results of the forces are constant. To an extent, it can be said that clearance angles do not much affect the cutting forces. This statement agrees with the experimental results obtained by An et al. [38]. They reported that a larger clearance angle caused lower cutting forces induced by orthogonal cutting. An et al. [38] concluded that with a smaller clearance angle, the machined surface was prone to contact with the tool clearance face, resulting in friction and extrusion, which can increase the cutting forces. In Figure 19, the variation of the maximum cutting forces and tool temperatures at various clearance angles is presented. It is clearly observed that the clearance angle has a negligible impact on the temperature and main cutting forces but affects the thrust forces slightly.

The instantaneous workpiece temperature results at various clearance angles are shown in Figure 20. From that figure, it is observable as to how the workpiece temperature suddenly increases when the tool strikes and permeates the material. The large friction occurring between the tool–workpiece interface promotes the increase in the forces and cutting temperature. After a few times, the machined surface cools down and reaches a value close to the room temperature and stays constant up to the cutting time.

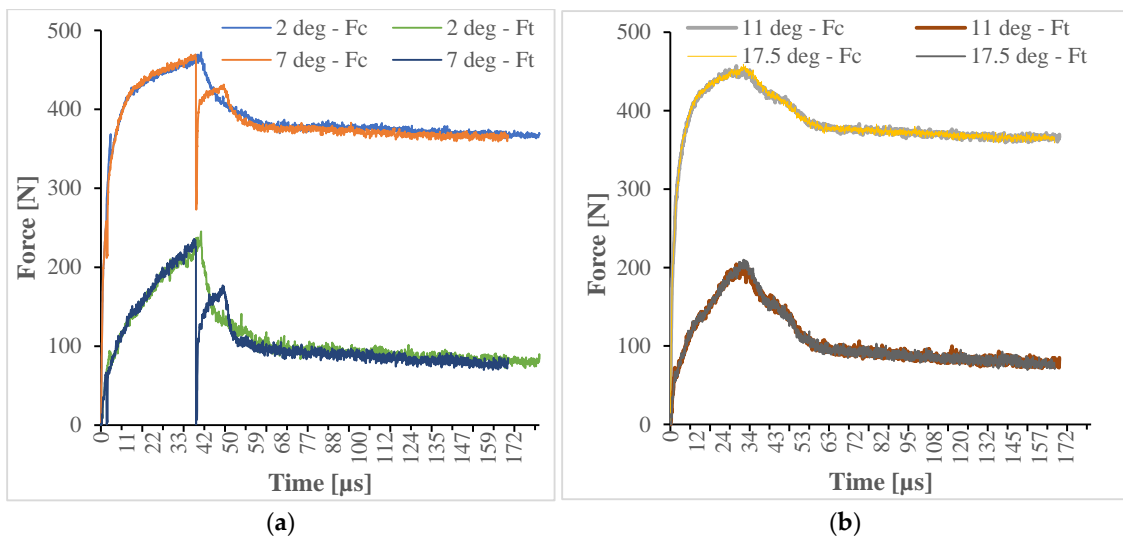


Figure 18. Force distribution during cutting process for different clearance angles ( $\alpha = 7^\circ$  and  $\gamma = 17.5^\circ$ ): (a) 2–7° and (b) 11–17.5°.

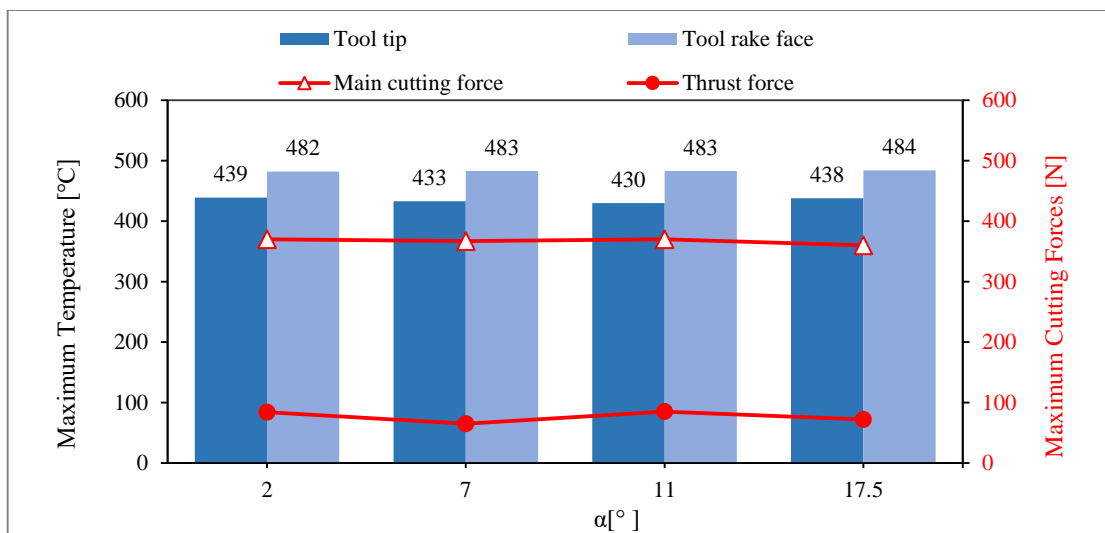


Figure 19. Maximum cutting temperatures and forces at various clearance angles.

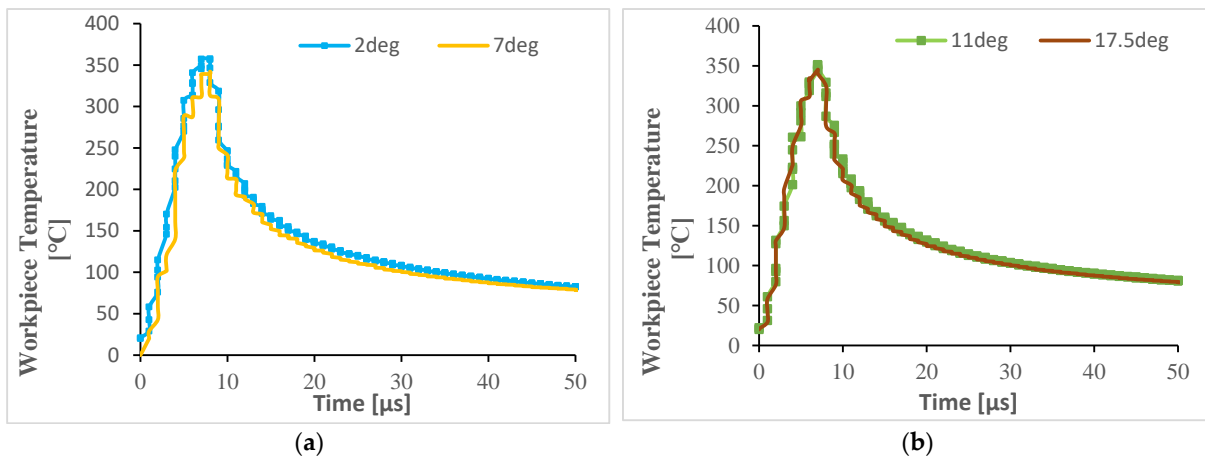
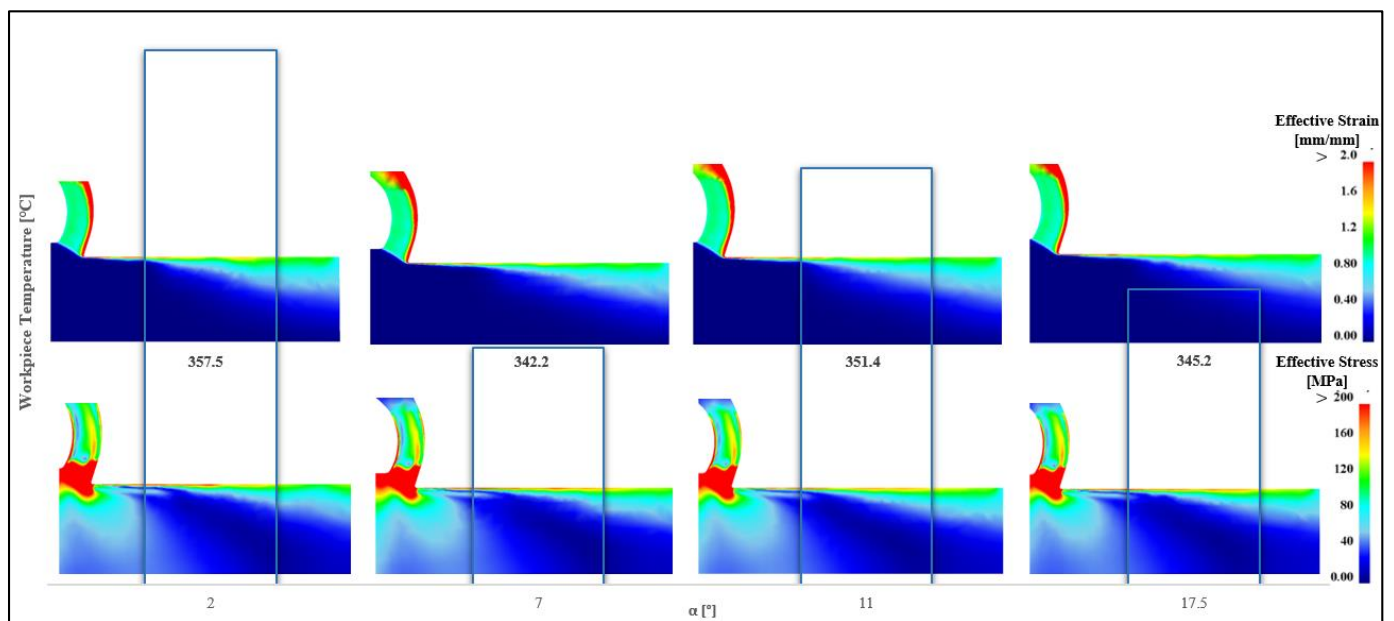


Figure 20. Effect of clearance angle on cutting temperature ( $r_e = 20 \mu\text{m}$  and  $\gamma = 17.5^\circ$ ): (a) 2–7° and (b) 11–17.5°.

Figure 21 shows the variation of strain, stress, and the largest instantaneous workpiece temperatures with respect to the clearance angles. It is observed that the workpiece temperature, effective strain, and stresses are inversely proportional to the clearance angles, although only for some ranges. However, a direct proportionality between temperature-effective strain-effective stress and the clearance angle is observed from  $7^\circ$  to  $11^\circ$ . However, the variation of the responses for each angle are less than 20%. From this investigation, the effect of the clearance angle in orthogonal cutting can be neglected. Nevertheless, more investigations are necessary. The proposal to vary both the rake and clearance angle at the same time would aid in better understanding the interactions among the tool geometry and machine parameters.



**Figure 21.** Maximum workpiece temperature strain–stress simulation with respect to the clearance angle.

### 3.3.2. Effect of the Clearance Angle on Residual Stresses

The effects of the clearance angles on the residual stresses are observed in Figure 22. From the results, it is observed that as the clearance angle grows from  $2^\circ$  to  $7^\circ$  the surficial residual stresses decrease whereas from  $7^\circ$  to  $17.5^\circ$ , they increase. In Figure 23, the graphs of the residual stresses distribution from the machined workpiece are illustrated.

In Figure 23, tensile residual stresses are observed at the machined surface. From a depth below 0.3 mm, compressive residual stresses are obtained. Moreover, the residual stress behavior does not seem to vary much for all the tested clearance angles ( $2^\circ$  to  $17.5^\circ$ ). The minimum obtained value of compressive residual stresses is about  $-15$  MPa. Future investigations will be conducted to understand possible interactions between the tool edge radius, clearance, rake angle, and machining parameters on residual stresses.

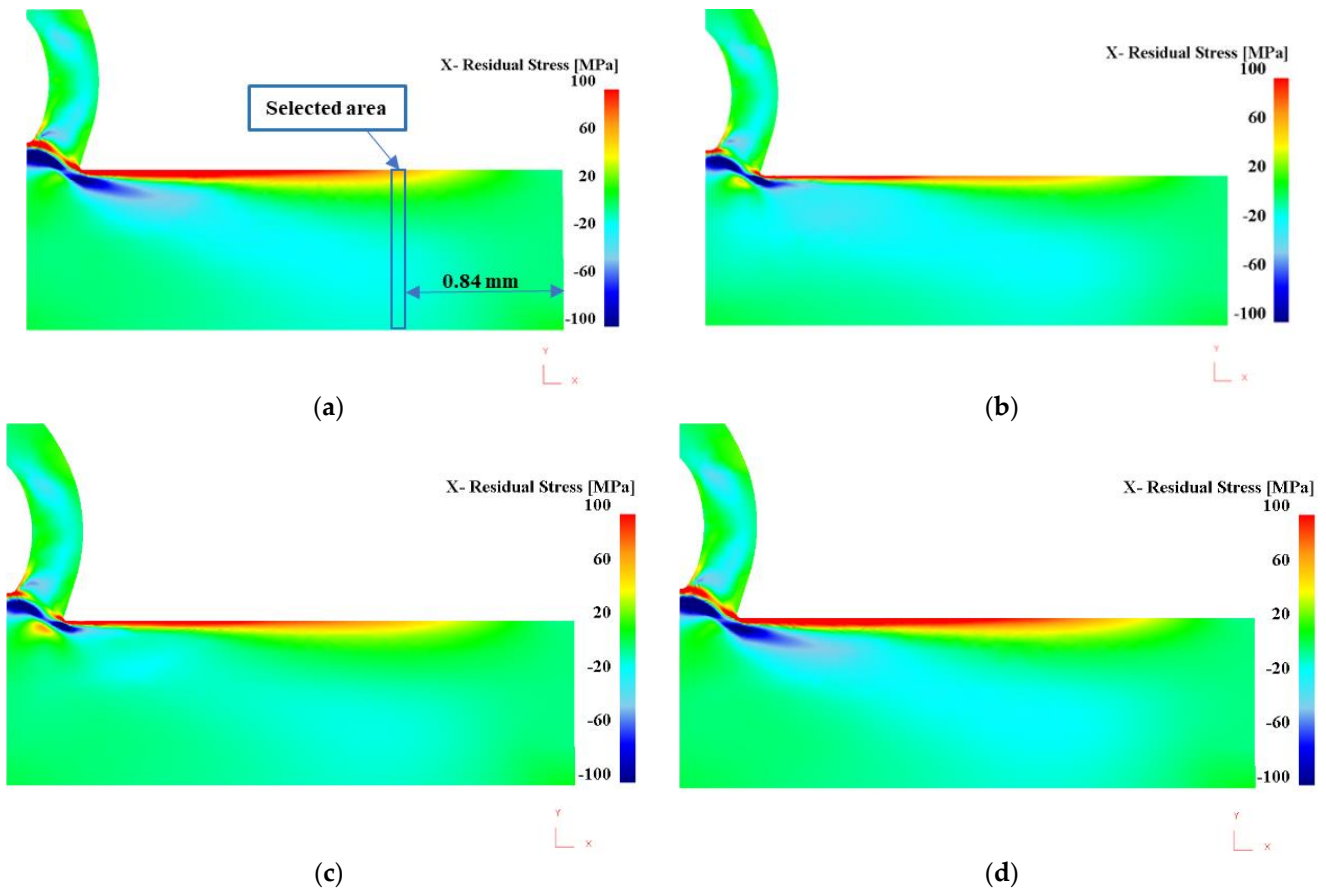


**Figure 22.** Simulation results of residual stresses measurement in the workpiece depth ( $r_\epsilon = 20 \mu\text{m}$  and  $\gamma = 17.5^\circ$ ): (a)  $2^\circ$ , (b)  $7^\circ$ , (c)  $11^\circ$ , and (d)  $17.5^\circ$ .

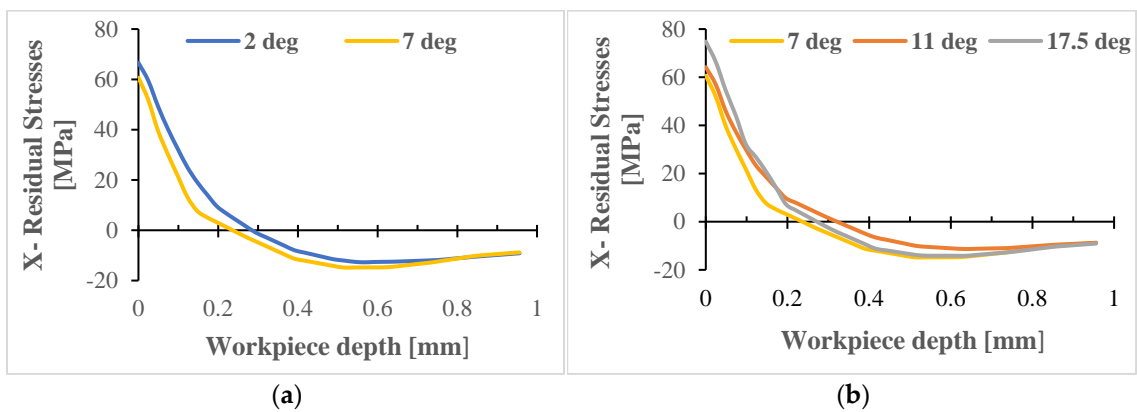


**Figure 23.** Effect of the clearance angle on the axial X-residual stresses ( $r_\epsilon = 20 \mu\text{m}$ ). (a)  $2\text{--}7^\circ$ ; (b)  $7\text{--}17.5^\circ$ .

### 3.4. Discussion

In the previous sections the effects of the tool edge radius, rake angle, and clearance angle on the temperatures (tool and workpiece), forces, and residual stresses were discussed. Figures 24 and 25 summarize the influence of these tool geometry parameters on the maximum surface residual stresses and on the minimum residual stresses. It appears that the edge radius is the most influential factor (Figures 24c and 25c) followed by the rake angle. This can be explained by the fact that the temperature and the forces on the workpiece and the forces increase with nose radius (Figure 6) while, the temperature and

the forces decrease when using a tool with a positive rake angle (Figure 13). A compromise must be made when selecting the tool edge radius and the rake angle.

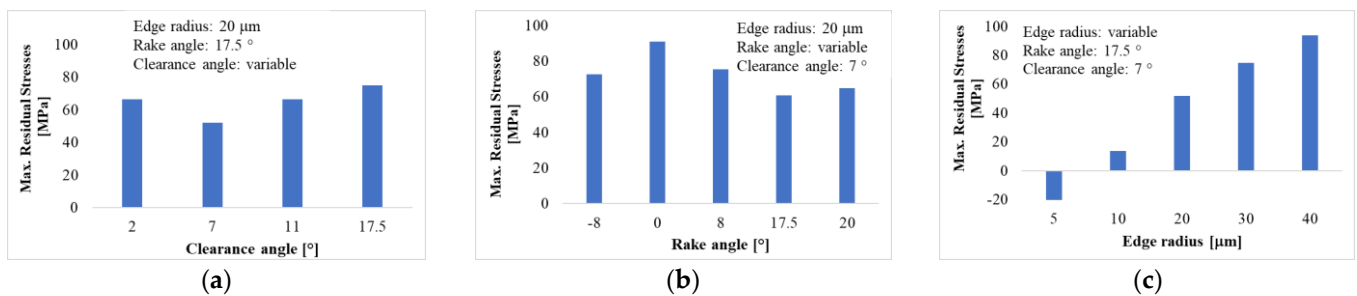


**Figure 24.** Effects of tool geometry on maximum residual stress: (a) clearance angle, (b) rake angle, and (c) nose radius.

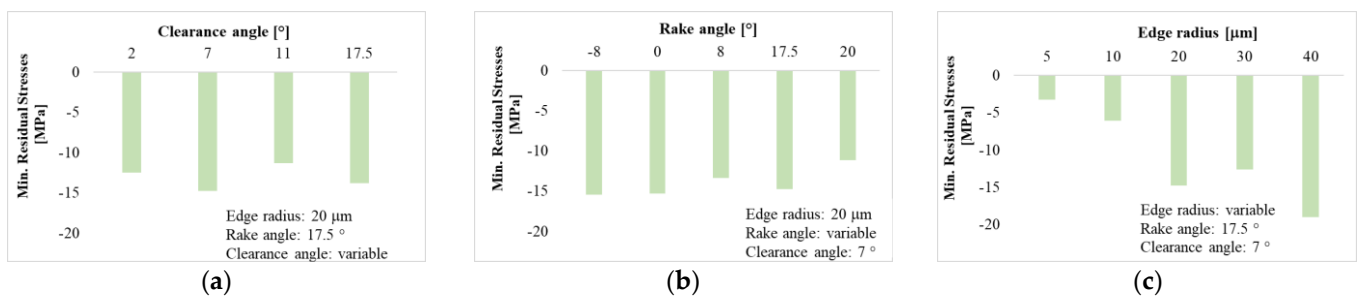


**Figure 25.** Effects of the tool geometry on minimum residual stress: (a) clearance angle, (b) rake angle, and (c) nose radius.

The effect of the clearance angle on residual stresses is not clear (Figures 24 and 25a). The maximum cutting temperature and the cutting forces remain almost constant when varying the clearance angle (Figure 19). The obtained residual stresses are a compressive type from a depth of 0.3 mm below the surface (Figures 10, 17 and 23). Therefore, a finishing operation at a cutting depth greater than 0.5 mm using a tool with a small edge radius (e.g., 0.005 mm) can eliminate the initial tension stresses on the surface of the part and generate compression stresses that are favorable for the fatigue life of the part.

### 3.5. Results Validation

Figure 26 shows the comparison of the simulated cutting forces and experimental test results obtained by Daoud et al. [33]. These experiments were conducted on AA6061-T6, using orthogonal turning with a cutting speed of 950 m/min and a feed of 0.16 mm/rev. XR diffraction was used in the experimental tests that were used to validate our simulated results (see previous publications by the authors: Javidikia et al. [5] and Jomaa et al. [39]). Even though the simulated cutting forces (Figure 26) were obtained for a 17.5° rake angle, while the tests were conducted on a rake angle of  $-8^\circ$  to  $+8^\circ$ , the simulation results are comparable to those obtained by Daoud [33]. Moreover, the cutting temperature data (simulations and experiments), as a function of rake angles, correlate well (Figure 27).

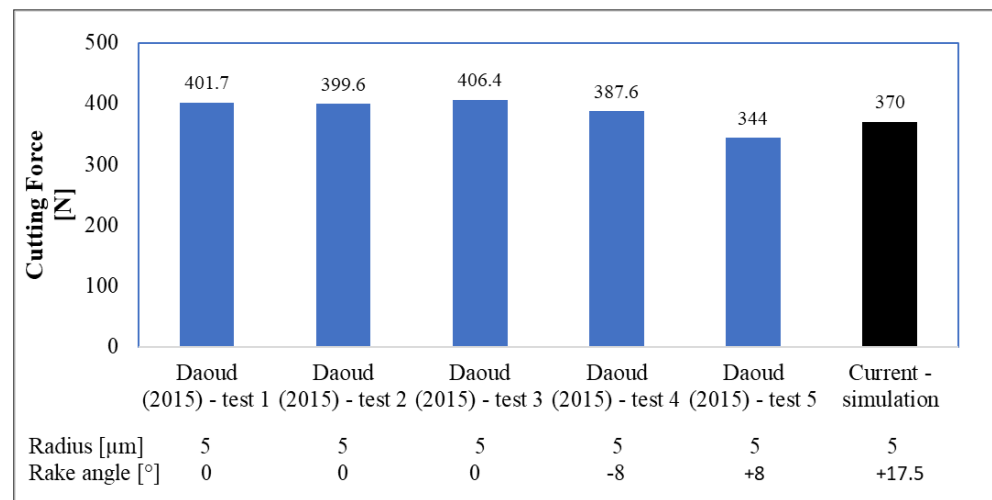


Figure 26. Comparison of simulated cutting forces and experimental cutting forces [33].

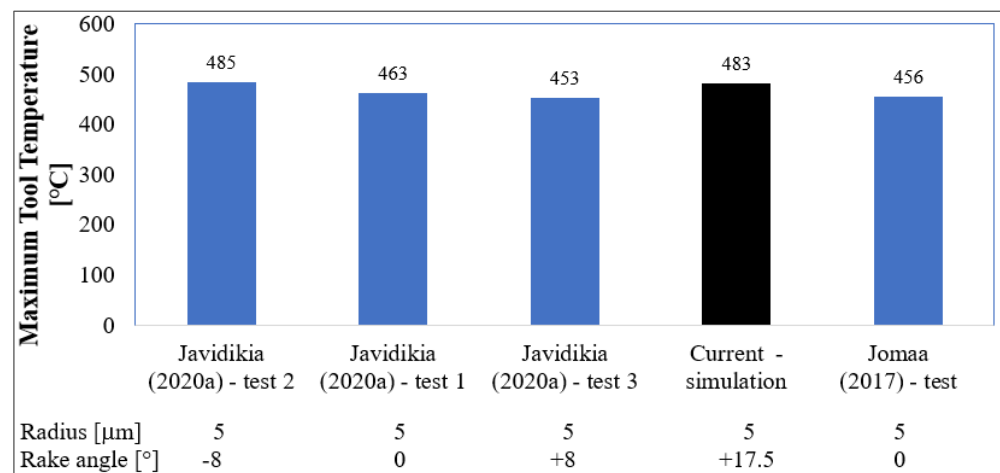


Figure 27. Comparison of simulated temperature and experimental temperature [5,39].

In Table 5, the experimental results of the cutting force, thrust force, temperatures, and residual stresses obtained by Javidikia et al. [3] are compared with the simulations. It is found that the values of the cutting temperature and residual stresses are comparable. The errors compared to the results obtained are below 20%. The discrepancies in the results could be justified by the high friction coefficient used in the simulations. In addition to that, the material constitutive model used in DEFORM™ might not exactly match the actual behavior of the material during the machining. Moreover, the friction model used may require more investigation. Developing studies that could incorporate the interactive effects of tool geometry parameters and machining conditions would be relevant for future work.

Table 5. Comparison of simulated results and experimental data obtained by Javidikia et al. [3].  $V = 950 \text{ mm/min}$ ,  $f = 0.16 \text{ mm/min}$ , rake angle  $17.5^\circ$ , and clearance angle  $7^\circ$ .

Authors	Cutting Forces (N)	Thrust Force (N)	Temperature ( $^\circ$ )	Residual Stress (MPa)
Javidikia et al. [3]	384	77	473	55
Current simulation	367	65	483	60.6
Errors	4%	16%	-2%	-10%

This research work has demonstrated that the tool geometry can be selected to promote compressive residual stresses on the workpiece and therefore improves the fatigue life of the component. The residual stress state could be improved using surface treatment such as burnishing, grinding, shot peening, or by laser peening [40], although they are costly additional processes. Boozarpour et al. [15] shown that positive residual stress on a turned AA 6061-T6 could be reversed into high compressive stress in the surface part and beneath the surface (up to 0.6 mm depth), and that resulted in extending the fatigue life of the part by a factor of three. Similar work was optimized by El Axir et al. [16] during the burnishing process on AA6061-T6. They obtained an improved fatigue life about twice better than the original turning process. The best residual stresses occurred at an 800 MPa distance 250  $\mu\text{m}$  below the surface. Rodriguez et al. [17] demonstrated that roll burnishing can improve the surface finish and introduce compressive residual stress in the machined workpiece. Their results obtained on steel were comparable to ball burnishing results.

#### 4. Conclusions

Numerical investigations were conducted to study the impact of tool geometry (edge radius, rake, and clearance angles) parameters on thermomechanical loads and residual stresses induced by the orthogonal cutting of AA6061-T6. The results showed that:

- The state of residual stresses and the thermo-mechanical loads on the machined parts and cutting tools depend on the tool geometry used and more specially on tool edge radius and rake angle. A larger edge radius, for example, can lead to lower cutting forces and temperatures, but may also result in higher residual stresses. The cutting temperature, workpiece temperature, and cutting forces were found proportional to the edge radius. Higher compressive residual stresses were obtained for a 5  $\mu\text{m}$  tool edge radius, but these results depend on the rake angle used. Hence, there is a need to optimize these tool geometries to obtain compressive residual stresses on the workpiece surface and beneath;
- As the rake angle increased from negative to positive, the cutting temperature, cutting forces, effective strain, and stresses decreased considerably. The steady workpiece temperature and residual stresses were proportional to the rake angles for positive angles and were inversely proportional to positive rake angles. The rake angles of  $0^\circ$  and  $17.5^\circ$  were found to produce more compressive stresses inside the workpiece material;
- It has been shown that the rake angle and the tool edge radius are the two parameters that most affect the state of the residual stresses on the workpiece. Generally, these stresses are compression type from a depth of 0.3 mm below the surface. Therefore, a finishing operation at a cutting depth greater than 0.5 mm using a tool with a small edge radius (e.g., 0.005 mm) can eliminate the initial tension stresses on the surface of the part and generate compression stresses that are favorable for the fatigue life of the part;
- Finally, it was found that varying the tool clearance angle from 2 to 17.5 degrees has no significant effect on the temperature, forces, effective strain, effective stresses, and residual stresses during orthogonal turning of AA6061-T6. The impact of clearance angle variation on thermal mechanical load and stresses for this application can be neglected;
- The future work will focus on the optimization of tool geometry and machining parameters to achieve desired residual stresses.

**Author Contributions:** Conceptualization and methodology, S.A.T.T. and M.J. (Mahshad Javidikia); software, S.A.T.T. and M.J. (Mahshad Javidikia); technical discussion and result analysis, V.S., S.A.T.T. and M.J. (Mahshad Javidikia); project investigation, S.A.T.T.; writing—original draft preparation, S.A.T.T.; resources, supervision, and writing—review and editing, V.S. and M.J. (Mohammad Jahazi); final revision and editing, V.S., M.J. (Mohammad Jahazi) and S.A.T.T. All authors have read and agreed to the published version of the manuscript.

**Funding:** This research received no external funding. The APC was funded by Victor Songmene’s research fund.

**Institutional Review Board Statement:** Not applicable.

**Informed Consent Statement:** Not applicable.

**Data Availability Statement:** Data is available on request due to restrictions privacy or ethical.

**Acknowledgments:** The authors would like to thank the Aluminum Research Centre (REGAL) for financially supporting the doctoral studies of the first author. They would also like to acknowledge SFTC DEFORM™ for their technical support. Many thanks also go to Irfan Ullah for constructive discussions.

**Conflicts of Interest:** The authors declare no conflict of interest.

## References

1. Sadeghifar, M.; Sedaghati, R.; Songmene, V. FE modeling and optimization of cutting temperature in orthogonal turning. *Simulation* **2016**, *922*, 178.
2. Songmene, V.; Khettabi, R.; Zaghbani, I.; Kouam, J.; Djebar, A. Machining and Machinability of Aluminum Alloys. In *Aluminium Alloys, Theory and Applications*; Kvackaj, T., Ed.; IntechOpen: London, UK, 2011. [CrossRef]
3. Javidikia, M.; Sadeghifar, M.; Songmene, V.; Jahazi, M. Low and High Speed Orthogonal Cutting of AA6061-T6 under Dry and Flood-Coolant Modes: Tool Wear and Residual Stress Measurements and Predictions. *Materials* **2021**, *14*, 4293. [CrossRef] [PubMed]
4. Javidikia, M.; Sadeghifar, M.; Songmene, V.; Jahazi, M. Effect of turning environments and parameters on surface integrity of AA6061-T6: Experimental analysis, predictive modeling, and multi-criteria optimization. *Int. J. Adv. Manuf. Technol.* **2020**, *110*, 2669–2683. [CrossRef]
5. Javidikia, M.; Sadeghifar, M.; Songmene, V.; Jahazi, M. On the impacts of tool geometry and cutting conditions in straight turning of aluminum alloys 6061-T6: An experimentally validated numerical study. *Int. J. Adv. Manuf. Technol.* **2020**, *106*, 4547–4565. [CrossRef]
6. Ravikanth, D.; Reddy, K.P.; Murthy, V.S.S. Influence of tool geometry on cutting zone temperature during turning of aluminium alloy AA2219. *Mater. Today Proc.* **2022**, *62*, 2277–2282. [CrossRef]
7. Casuso, M.; Rubio-Mateos, A.; Veiga, F.; Lamikiz, A. Modeling of cutting force and final thickness for low stiffness 2024-T3 aluminum alloy part milling considering its geometry and fixtures. *J. Mater. Res. Technol.* **2022**, *21*, 2416–2427. [CrossRef]
8. Daoud, M.; Chatelain, J.; Bouzid, H. On the Effect of Johnson Cook Material Constants to Simulate Al2024-T3 Machining Using Finite Element Modeling. In Proceedings of the ASME 2014 International Mechanical Engineering Congress and Exposition, Volume 2A: Advanced Manufacturing, Montreal, QC, Canada, 14–20 November 2014. V02AT02A044. ASME. [CrossRef]
9. Patel, J. Finite Element Studies of Orthogonal Machining of Aluminum Alloy A2024-T351. UNC Charlotte Electron. Theses Diss. 2018. Available online: <https://ninercommons.charlotte.edu/islandora/object/etd%3A318/> (accessed on 12 May 2022).
10. Daoud, M.; Chatelain, J.F.; Bouzid, A. Effect of rake angle on Johnson-Cook material constants and their impact on cutting process parameters of Al2024-T3 alloy machining simulation. *Int. J. Adv. Manuf. Technol.* **2015**, *81*, 1987–1997. [CrossRef]
11. Jomaa, W.; Daoud, M.; Songmene, V.; Bocher, P.; Châtelain, J. Identification and Validation of Marusich’s Constitutive Law for Finite Element Modeling of High Speed Machining. In Proceedings of the ASME 2014 International Mechanical Engineering Congress and Exposition, Volume 2A: Advanced Manufacturing, Montreal, QC, Canada, 14–20 November 2014. V02AT02A057. ASME. [CrossRef]
12. Aurrekoetxea, M.; de Lacalle, L.N.L.; Zelaieta, O.; Llanos, I. Uncertainty Assessment for Bulk Residual Stress Characterization Using Layer Removal Method. *Exp. Mech.* **2023**, *63*, 323–335. [CrossRef]
13. Aurrekoetxea, M.; Llanos, I.; Zelaieta, O.; de Lacalle, L.N.L. Towards advanced prediction and control of machining distortion: A comprehensive review. *Int. J. Adv. Manuf. Technol.* **2022**, *122*, 2823–2848. [CrossRef]
14. Sadeghifar, M.; Javidikia, M.; Loucif, A.; Jahazi, M.; Songmene, V. Experimental and numerical analyses of residual stress redistributions in large steel dies: Influence of tempering cycles and rough milling. *J. Mater. Res. Technol.* **2023**, *24*, 395–406. [CrossRef]
15. Boozarpoor, M.; Teimouri, R. Parametric study of multi-roller rotary burnishing process. *Int. J. Lightweight Mater. Manuf.* **2021**, *4*, 179–194. [CrossRef]
16. El-Axir, M.H. An investigation into the ball burnishing of aluminium alloy 6061-T6. *Proc. Inst. Mech. Eng. Part B J. Eng. Manuf.* **2007**, *221*, 1733–1742. [CrossRef]
17. Rodriguez, A.; de Lacalle, L.N.L.; Pereira, O.; Fernandez, A.; Ayesta, I. Isotropic finishing of austempered iron casting cylindrical parts by roller burnishing. *Int. J. Adv. Manuf. Technol.* **2020**, *110*, 753–761. [CrossRef]
18. Teimouri, R.; Amini, S.; Bami, A.B. Evaluation of optimized surface properties and residual stress in ultrasonic assisted ball burnishing of AA6061-T6. *Measurement* **2018**, *116*, 129–139. [CrossRef]

19. Nasr, M.N.A.; Ng, E.-G.; Elbestawi, M.A. Modelling the effects of tool-edge radius on residual stresses when orthogonal cutting AISI 316L. *Int. J. Mach. Tools Manuf.* **2007**, *47*, 401–411. [[CrossRef](#)]
20. Aich, Z.; Haddouche, K.; Djellouli, K.; Ghezal, A. An improved thermomechanical modeling for orthogonal cutting of AISI 1045 steel. *Results Eng.* **2023**, *17*, 100789. [[CrossRef](#)]
21. Tagiuri, Z.A.M.; Dao, T.-M.; Samuel, A.M.; Songmene, V. A Numerical Model for Predicting the Effect of Tool Nose Radius on Machining Process Performance during Orthogonal Cutting of AISI 1045 Steel. *Materials* **2022**, *15*, 3369. [[CrossRef](#)]
22. Navas, V.G.; Gonzalo, O.; Bengoetxea, I. Effect of cutting parameters in the surface residual stresses generated by turning in AISI 4340 steel. *Int. J. Mach. Tools Manuf.* **2012**, *61*, 48–57. [[CrossRef](#)]
23. Özel, T. Experimental and Finite Element Investigations on the Influence of Tool Edge Radius in Machining Nickel-Based Alloy. In Proceedings of the ASME 2009 International Manufacturing Science and Engineering Conference, West Lafayette, IN, USA, 4–7 October 2009; pp. 493–498. [[CrossRef](#)]
24. Jomaa, W.; Songmene, V.; Bocher, P. Surface Finish and Residual Stresses Induced by Orthogonal Dry Machining of AA7075-T651. *Materials* **2014**, *7*, 1603–1624. [[CrossRef](#)]
25. Cheng, X.; Zha, X.; Jiang, F. Optimizing the geometric parameters of cutting edge for rough machining Fe-Cr-Ni stainless steel. *Int. J. Adv. Manuf. Technol.* **2016**, *85*, 683–693. [[CrossRef](#)]
26. Reddy, M.M.; Kumar, M.; Shanmugam, K. Finite element analysis and modeling of temperature distribution in turning of titanium alloys. *Met. Mater. Eng.* **2018**, *24*, 59–69. [[CrossRef](#)] [[PubMed](#)]
27. Liu, Y.; Xu, D.; Agmell, M.; M'Saoubi, R.; Ahadi, A.; Stahl, J.-E.; Zhou, J. Numerical and experimental investigation of tool geometry effect on residual stresses in orthogonal machining of Inconel 718. *Simul. Model. Pract. Theory* **2021**, *106*, 102187. [[CrossRef](#)]
28. Salman, K.H.; Elsheikh, A.H.; Ashham, M.; Ali, M.K.A.; Rashad, M.; Haiou, Z. Effect of cutting parameters on surface residual stresses in dry turning of AISI 1035 alloy. *J. Braz. Soc. Mech. Sci. Eng.* **2019**, *41*, 349. [[CrossRef](#)]
29. Li, P.; Chang, Z. Numerical Modeling of the Effect of Cutting-Edge Radius on Cutting Force and Stress Concentration during Machining. *Micromachines* **2022**, *13*, 211. [[CrossRef](#)] [[PubMed](#)]
30. Rao, K.S.S.; Allamraju, K.V. Effect on Micro-Hardness and Residual Stress in CNC Turning of Aluminium 7075 Alloy. *Mater. Today Proc.* **2017**, *4*, 975–981. [[CrossRef](#)]
31. Sadeghifar, M.; Sedaghati, R.; Jomaa, W.; Songmene, V. A comprehensive review of finite element modeling of orthogonal machining process: Chip formation and surface integrity predictions. *Int. J. Adv. Manuf. Technol.* **2018**, *96*, 3747–3791. [[CrossRef](#)]
32. Yen, Y.-C.; Jain, A.; Chigurupati, P.; Wu, W.-T.; Altan, T. Computer Simulation of Orthogonal Cutting using a Tool with Multiple Coatings. *Mach. Sci. Technol.* **2004**, *8*, 305–326. [[CrossRef](#)]
33. Daoud, M.; Jomaa, W.; Chatelain, J.F.; Bouzid, A. A machining-based methodology to identify material constitutive law for finite element simulation. *Int. J. Adv. Manuf. Technol.* **2015**, *77*, 2019–2033. [[CrossRef](#)]
34. Sadeghifar, M.; Javidikia, M.; Songmene, V.; Jahazi, M. Finite element simulation-based predictive regression modeling and optimum solution for grain size in machining of Ti6Al4V alloy: Influence of tool geometry and cutting conditions. *Simul. Model. Pract. Theory* **2020**, *104*, 102141. [[CrossRef](#)]
35. Giang, L.H. Investigation of Effects of Tool Geometry Parameters on Cutting Forces, Temperature and Tool Wear in Turning Using Finite Element Method and Taguchi's Technique. *IJMEA* **2016**, *4*, 109. [[CrossRef](#)]
36. Choi, Y. Influence of rake angle on surface integrity and fatigue performance of machined surfaces. *Int. J. Fatigue* **2017**, *94*, 81–88. [[CrossRef](#)]
37. Liao, Z.; la Monaca, A.; Murray, J.; Speidel, A.; Ushmaev, D.; Clare, A.; Axinte, D.; M'Saoubi, R. Surface integrity in metal machining—Part I: Fundamentals of surface characteristics and formation mechanisms. *Int. J. Mach. Tools Manuf.* **2021**, *162*, 103687. [[CrossRef](#)]
38. An, Q.; Ming, W.; Cai, X.; Chen, M. Effects of tool parameters on cutting force in orthogonal machining of T700/LT03A unidirectional carbon fiber reinforced polymer laminates. *J. Reinf. Plast. Compos.* **2015**, *34*, 591–602. [[CrossRef](#)]
39. Jomaa, W.; Songmene, V.; Bocher, P.; Gakwaya, A. FEA-Based Comparative Investigation on High Speed Machining of Aluminum Alloys AA6061-T6 and AA7075-T651. *Solid State Phenom.* **2017**, *261*, 347–353. [[CrossRef](#)]
40. Huang, K.; Yang, W. Analytical modeling of residual stress formation in workpiece material due to cutting. *Int. J. Mech. Sci.* **2016**, *114*, 21–34. [[CrossRef](#)]

**Disclaimer/Publisher's Note:** The statements, opinions and data contained in all publications are solely those of the individual author(s) and contributor(s) and not of MDPI and/or the editor(s). MDPI and/or the editor(s) disclaim responsibility for any injury to people or property resulting from any ideas, methods, instructions or products referred to in the content.